UNIVERSITÀ POLITECNICA DELLE MARCHE
FACOLTÀ DI INGEGNERIA

CORSO DI LAUREA TRIENNALE IN INGEGNERIA INFORMATICA E DELL'AUTOMAZIONE

Simulazione ed implementazione di tecniche di controllo per il riorientamento e il docking autonomi di uno spacecraft

Simulation and design of control techniques for autonomous reorientation and docking of a spacecraft

Relatore:
Prof. Simone Fiori

Laureando:
Edoardo Sampaolesi

A.A. 2022/2023

Abstract

The aim of the present thesis is to propose a framework to model, simulate and control a small spacecraft in the proximity of a space station through manifold calculus. In particular, two maneuvers are modeled and simulated, namely reorientation under directional constraints and rendezvous in the presence of physical obstacles. The mathematical model of the roto-translational motion of a spacecraft as well as the design of control fields are entirely written by coordinate-free Lie-group-type formulations. A number of numerical experiments complement the theoretical endeavor, illustrate the achieved progress and guide the reader through an evaluation of the most convenient control strategy.

Sommario

L'attuale progetto affronta lo sviluppo di tecniche di controllo per veicoli spaziali di piccole dimensioni attraverso l'applicazione della teoria dei manifold e dei campi potenziali artificiali. In particolare, sono due le manovre prese in considerazione: il riorientamento con vincoli direzionali e il rendezvous in presenza di ostacoli fisici.

Più nel dettaglio, il riorientamento con vincoli direzionali consiste nell'assicurare che eventuali strumentazioni montate a bordo del veicolo spaziale si mantengano direzionate all'interno di aree definite obbligatorie, come per esempio il mantenimento del contatto radio di antenne montate a bordo, mentre altre si mantengano al di fuori di zone definite proibite, tale problema riguarda particolari strumentazioni sensibili a forti intensità luminose come alcuni telescopi soggetti alla luce solare; il rendezvous in presenza di ostacoli fisici consiste nell'assicurare l'avvicinamento di un veicolo spaziale a un altro evitando gli ostacoli presenti, questi possono essere: detriti spaziali, zone di comunicazione radio o altri veicoli spaziali, solitamente a una fase di rendezvous segue una fase di docking la quale porta i due veicoli spaziali ad agganciarsi, anche la fase di docking è oggetto di studio di tale progetto.

Lo scopo finale di tale progetto è quello di suggerire quale fra le tecniche proposte in seguito è la migliore secondo delle metriche considerate dall'autore, fra le quali la traiettoria compiuta e la quantità di carburante utilizzato.

Le tecniche proposte si basano sulla teoria dei manifold e la definizione di campi potenziali artificiali, questi ultimi sono stati articolati in due componenti principali: le zone attrattive, necessarie per attrarre il soggetto verso un punto di arrivo voluto, sia per la manovra di rendezvous che per quella di riorientamento, e le zone repulsive, definite in prossimità di ostacoli, che servono per deviare la traiettoria al di fuori di aree proibite.

In seguito alla modellazione si è passato alla simulazione e confronto fra le varie soluzioni proposte, sono stati eseguiti diversi esperimenti, simulati, prendendo in considerazione situazioni differenti per evidenziare le criticità e le qualità di ogni algoritmo di controllo.

Infine, le conclusioni commentano i risultati ottenuti e suggeriscono future prospettive di approfondimento.

Contents

List of Figures

List of Tables

Chapter 1

Introduction

1.1 Autonomous rendezvous

Autonomous guidance of small-sized unmanned spacecrafts has been a goal in applied research since the inception of space missions. Autonomous guidance is able to overcome communications delays with the ground guidance station while benefiting from direct on-site obstacle sensing and avoidance.

Current and future orbital missions involve operations in the proximity of large space structures, such as the International Space Station [1]. A view of the International Space Station is reproduced in Figure 1.1. Rendezvous operations constitute a vital step in unmanned spacecrafts missions to extend their operational life, as they allow on-orbit refueling of cold gas propellants and maintenance [2]. Rendezvous may be broken down into a *cruising phase*, during which the spacecraft leaves its orbit to approach the space station, and a *docking phase*, which starts a few dozens of meters away from the station and leads the spacecraft to physically conjoin the space station through one of the available docking ports.

Figure 1.1: A view of the International Space Station (ISS).

Source: `wikimedia.org`

While the docking phase concerns precision guidance and collision avoidance with the space station, guidance along the cruising phase is heavily affected by physical obstacles which may be moving or fixed with respect to the station and the spacecraft. Obstacles may be active satellites, micrometeoroids or space debris, parts of vehicles arisen from collisions still in orbit around the Earth. A serious accident on records happened in February 2009, when Iridium-33 communication satellite and Kosmos-2251 (non-operating) military satellite accidentally collided [3] at an altitude of 776 km above the territory of Siberia at a speed of 11.7 km/s. Both satellites were destroyed in the impact producing more than 2,300 fragments. One third of such fragments entered the atmosphere and disintegrated, while the rest is still orbiting the Earth today. A large number of space debris orbiting the Earth are currently being watched upon by NASA through the Orbital Debris Program Office whose logo is reproduced in Figure 1.2.

Figure 1.2: Logo of the Orbital Debris Program Office (ODPO).

Source: `orbitaldebris.jsc.nasa.gov`.

1.2 Reorientation under directional constraints

Reorientation of a spacecraft is likewise a fundamental operation to be carried out during an exploratory mission. Large-angle attitude slew maneuvers are required to achieve retargeting of payload instrumentation during science missions [4]. Reorientation from one direction to another must be operated in such a way that the boresight of sensitive instrumentation, such as cryogenically cooled infrared telescope [4] and star sensor [5], is not directed toward any bright object such as the Sun, the Earth or the Moon, while the antenna does not lose communication with the ground or the station [6]. In particular, boresight evasion introduces the notion of attitude forbidden constraints [5]. Automated reorientation in the presence of attitude constraints poses a challenging computational task for the on-board guidance control system [7].

Automated reorientation plays a crucial role even during the docking phase, since safe docking may take place only if the docking axis of the spacecraft is precisely oriented along the docking axis of the station docking port. In this phase, orientation is supposed to happen with extreme precision, facilitated by the alleged absence of directional obstructions.

1.3 Choice of mathematical representation of rotational dynamics

The mathematical representation to model the roto-translational dynamics of a spacecraft, as well as the control strategy to make a spacecraft execute the necessary movements in space, are a subject of continued debate in the scientific community. In particular, the mathematical representation of the rotational dynamics may be picked from the realms of Tait-Bryan representation, quaternions and rotation matrices. Tait-Bryan angles carry an intuitive and easy-to-visualize value [8], although the conversion from angular to Cartesian coordinate is burdened by complex trigonometric expressions and from inherent singularities [7]. Quaternion-based representations are often invoked in aerospace engineering [7], although quaternions are affected by the well-known problem of unwinding due to the redundancy of the unit quaternion (namely, when the rotation angle is sufficiently large, the trajectory of attitude maneuver may be longer, leading to increased propellant consumption and longer maneuver time) [5].

A distinguishing feature of the present thesis endeavor is that attitudes are represented through orthogonal rotation matrices and the corresponding control actions are represented through vector fields on the space of skew-symmetric matrices. These matrices are treated as a whole, without any need to resort to angles nor scalar velocities. Although inherently redundant, coordinate-free rotation-matrices representations result to be singularity free [9] and easy to manage in modeling and control design thanks to the underlying theory of Lie groups [10, 11, 12], hence, rotation-matrices representations are the mathematical tool of choice in the present thesis endeavor. A relation between quaternion and rotation-matrix representations is discussed in the Appendix.

1.4 Artificial potential fields

Automated control of rigid bodies, such as drones, satellites, ground robots as well as remotely operated underwater vehicles, may benefit from the theory of virtual attractive-repulsive potentials, which has been explored and extended across the decades [13, 16, 17, 18, 19, 20, 21, 22, 23, 14, 15]. Artificial-potential-based control relies on artificial potential functions constructed so as to assign a potential value to each point of the state space in a way that promotes state transition toward a set goal while demoting state transitions toward undesired obstructions. In

particular, is cited the paper [24] that revises and utilizes gradient-based control fields in conjunction with further physically-plausible forces, the paper [25] that extends the theory of virtual attractive-repulsive potential to control the rotational dynamics by Lie-group theory, and the paper [7] that introduces the notion of barrier-type potentials to control the attitudinal dynamics of a spacecraft (in quaternion representation).

The aim of the present thesis is to devise a complete navigation and attitude control strategy for a spacecraft bound to an orbital station to effect space missions and automated docking. After recalling the principal equations governing the motion of an orbital spacecraft, a control strategy is defined to effect reorientation under mandatory/forbidden directional constraints. In addition, is presented a multi-objective control strategy to make a spacecraft approach safely an orbital station, while avoiding still as well as moving obstacles, until the final guidance phase that guarantees collision-free docking with the correct attitude.

1.5 Overview of the thesis

The present document is organized as follows. Chapter 2 recalls necessary details from orbital dynamics, including the set of reference frames used to describe the equations of motion and the kinds of propulsion systems available within a small-sized spacecraft. Chapter 3 details the notion of spacecraft reorientation under directional constraints, with special emphasis on mandatory and forbidden cones of the celestial sphere. In this chapter, appropriate virtual attractive-repulsive potentials to achieve reorientation are presented along with related gradient-type control torque terms. Chapter 4 of this document discusses automated rendezvous with the main station by breaking down a rendezvous maneuver task into three subtasks, namely: cruising in the presence of obstacles, far-end docking and near-end docking. Each subtask is discussed and tackled separately through an appropriate control strategy adapted to the required degree of precision needed. The general control strategy follows a speed control paradigm, based on sliding mode control, aided by virtual attractive-repulsive potential theory. Chapter 5 illustrates the theoretical content of this thesis through an extensive series of numerical experiments based on several cases-of-study from the scientific literature. Chapter 6 concludes the document and suggests a number of possible improvements to the current endeavor to be tackled in future research projects.

Chapter 2

Reference frames, physical model and equations of motion of a spacecraft

The present chapter aims at recalling several essential details concerning the reference frames used to describe the equations of motion of a small-sized spacecraft, the type of physical actuators that govern such motion and a mathematical model of motion. The terminology that shall be used within this document is recalled as well.

2.1 Application scenario and reference frames

The scenario taken into consideration in the present thesis endeavor involves a main *station*, which is assumed to stay in a stable orbit around the Earth and to be controlled directly by a ground station or by on-board personnel and is hence operated independently. The scenario also involves a small-sized unmanned *spacecraft*, endowed with a sensor (e.g., a telescope) to achieve scientific missions, a communication device (e.g., a radio antenna) to keep in touch with the ground station and/or the main station, and an on-board autonomous control system that is able to provide appropriate navigation and control actions.

In the examined scenario, the spacecraft, whose control is the main subject of present investigation, is supposed to be endowed with two series of actuators, namely a series of cold-gas-based *reaction thrusters* that serve to control its translational dynamics, and a series of *reaction wheels* that serve to control its rotational dynamics [2]. It is assumed that the number and disposition of thrusters and wheels are appropriate to make the spacecraft fully operated, namely, to ensure that the control actions generated by the devised control algorithm find appropriate realization. To what concerns the cold gas ejecting thrusters, it is assumed that their thrust cannot be modulated and is either null (when 'off') or maximum (while 'on') as shown in Figure 2.1.

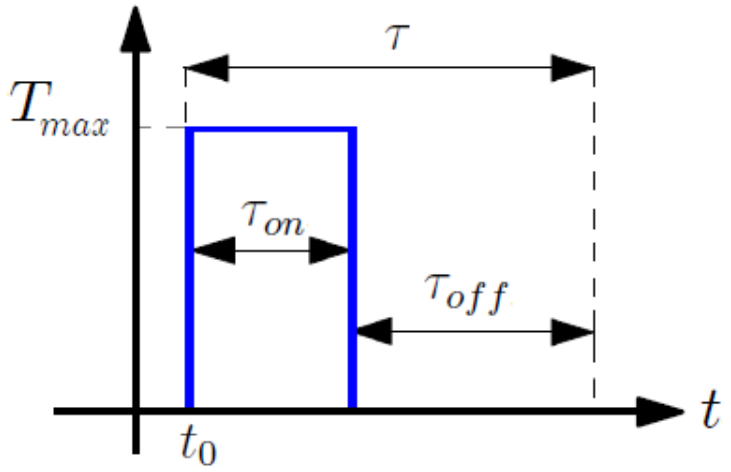

Figure 2.1: Visual representation of the thrust provided by a single thruster.

Source: [2]

Conversely, the spacecraft is assumed to be endowed with, at least, three reaction wheels (one per axis) through which it is possible to modulate any sort of active torque. (Special instances of under-actuated systems are studied, e.g., in [26].) A view of a small spacecraft is reproduced in Figure 2.2.

Figure 2.2: A pictorial view of a small-sized spacecraft.

Source: `https://www.nasa.gov`

An inertial reference frame $\mathcal{F}_{\mathrm{I}}$ is introduced to describe the direction of bright objects whose direct light exposure should be avoided, such as the Sun, the Earth, the Moon. The inertial reference frame $\mathcal{F}_{\mathrm{I}}$ is also necessary to specify the direction of a celestial object to be observed by a telescope, as well as the boresight of a transmitting antenna located on a main station. Such reference frame is introduced on the proviso that the mentioned directions stay constant within

the timespan of a given mission. Target attitudes, mandatory and forbidden pointing directions during reorientation maneuvers are referred to the frame $\mathcal{F}_{\mathrm{I}}$.

A station-fixed reference frame $\mathcal{F}_{\mathrm{S}}$ is also introduced. Such reference frame is integral with the space station and plays a fundamental role during rendezvous maneuvers and docking, in this phase the spacecraft takes as docking reference the orientation of the axis of the port that it is assigned to. In addition, during the cruising phase of rendezvous maneuver, the dynamics of the spacecraft is expressed in terms of the location of the station through the Clohessy-Wiltshire equations, which are valid for objects orbiting the Earth on circular orbits and that are spaced apart a few kilometers. The station-fixed reference frame $\mathcal{F}_{\mathrm{S}}$ is sometimes referred to as 'local vertical, local horizontal' (LVLH). Among the three orthogonal axes, one is directed from the center of the station to the center of the Earth ($\mathrm{R}_{\mathrm{bar}}$ or $\mathrm{Z}_{\mathrm{LVLH}}$) and is associated with a unit-vector $e_{\mathrm{z}} := [0\ 0\ 1]^{\top}$, one is directed tangentially to the orbit in the direction of motion ($\mathrm{V}_{\mathrm{bar}}$ or $\mathrm{X}_{\mathrm{LVLH}}$) and is associated with a unit-vector $e_{\mathrm{x}} := [1\ 0\ 0]^{\top}$. A third axis (labeled either $\mathrm{H}_{\mathrm{bar}}$ or $\mathrm{Y}_{\mathrm{LVLH}}$) is oriented so as to form a right-handed frame with the former two. The symbol $^{\top}$ denotes matrix transpose. A view of the LVLH reference frame is reproduced in Figure 2.3.

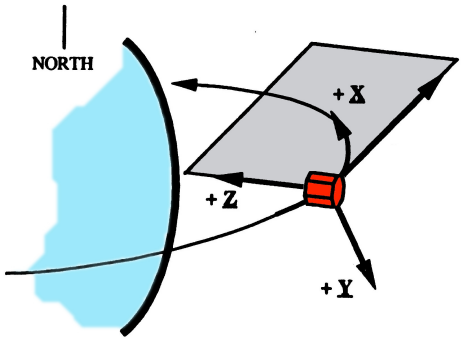

Figure 2.3: A pictorial view of the LVLH reference frame attached to a space station (in red color).

Source: `https://space.stackexchange.com`

A spacecraft-fixed reference frame $\mathcal{F}_{\mathrm{C}}$ is introduced as well, which describes the relative orientation and location of the spacecraft with respect to the inertial frame $\mathcal{F}_{\mathrm{I}}$ or the station-fixed frame $\mathcal{F}_{\mathrm{S}}$, depending on the maneuver being effected. (The subscript C stems from the fact that, in the rendezvous literature, the spacecraft is often referred to as *chaser*.) The Cartesian axes of the reference frame $\mathcal{F}_{\mathrm{C}}$ are assumed to be aligned to the principal axes of inertia of the spacecraft. The relative orientation and location enter the control goals to be fulfilled by the spacecraft.

2.2 Physical model and equations of motion

Under the assumption that the space station and the spacecraft are both orbiting the Earth at slightly different quotas, the translational motion of the spacecraft in the station-fixed reference frame $\mathcal{F}_{\mathrm{S}}$ may be described through the Clohessy-Wiltshire equations. The Clohessy–Wiltshire equations describe a simplified model of orbital relative motion, in which both the station and the spacecraft are in a circular orbit. The Clohessy–Wiltshire model provides a first-order approximation of the spacecraft's motion in a station-fixed reference frame [27].

Denoting by p the coordinate vector of the spacecraft with respect to the station-fixed reference frame $\mathcal{F}_{\mathrm{S}}$, the Clohessy–Wiltshire model reads

$$m\ddot{p} = f_{\mathrm{rt}} + f_{\mathrm{cc}} + f_{\mathrm{vd}} + f_{\mathrm{rd}},\ p(0) = p_0,\ \dot{p}(0) = v_0 \tag{2.1}$$

where the term f_{rt} denotes the resultant of the mechanical forces exerted by the reaction thrusters on the body of the spacecraft, f_{vd} denotes viscous drag due to friction with atmospheric particles, the term f_{cc} denotes the resultant of fictitious forces (Coriolis and centrifugal), f_{rd} denotes the resultant of random disturbances affecting the motion of the spacecraft and m denotes the total mass of the spacecraft at a given time.

The fictitious force term takes the expression:

$$f_{\mathrm{cc}} := m \begin{bmatrix} 0 & 0 & 0 \\ 0 & -\omega_0 & 0 \\ 0 & 0 & 3\omega_0^2 \end{bmatrix} p + m \begin{bmatrix} 0 & 0 & -2\omega_0 \\ 0 & 0 & 0 \\ -2\omega_0 & 0 & 0 \end{bmatrix} \dot{p} \tag{2.2}$$

where ω_0 denotes the orbital rate of the space station. For a circular orbit around a central body, the orbital rate is assumed to be constant and is evaluated through the expression $\omega_0 = \sqrt{\mu/r^3}$, where r denotes the radius of the circular orbit traveled by the station and μ denotes a standard gravitational parameter [28]. (In the present context, the standard gravitational parameter reads $\mu = G\,M_{\oplus}$, where G denotes the universal gravitational constant and $M_{\oplus}$ denotes the Earth's mass.)

The viscous drag is considered to be non-negligible only in the direction of motion (corresponding to the axis $\mathrm{V}_{\mathrm{bar}}$ of the LVLH system), hence the braking force takes the expression

$$f_{\mathrm{vd}} := -\tfrac{1}{2}\rho V_0^2 S C_{\mathrm{D}} e_{\mathrm{x}} \tag{2.3}$$

where ρ denotes the density of the atmosphere, V_0 denotes the orbital speed of the spacecraft, S denotes the frontal cross-section area of the spacecraft and C_{D} denotes a drag coefficient. The orbital speed may be written in terms of the orbital rate as $V_0 = r\,\omega_0$ and is henceforth constant.

All the other known perturbations can be considered orders of magnitude smaller than the drag force and so negligible.

Further forcing terms, essentially of random nature, are taken into account through the disturbance force f_{rd}.

To what concerns the rotational dynamics, the spacecraft is considered as a rigid body acted upon by a series of mechanical torques due to the reaction wheel and external disturbances. A constructive detail to bear in mind is that the thrusters are arranged in such a way that two thrusters at a time are eventually switched on in order to exert a null torque on the spacecraft body. Such design aids control development since it essentially decouples translational-oriented actuation from rotational-oriented actuation.

The attitude of a spacecraft with respect to the space station is quantified by a rotation matrix $R \in \mathrm{SO}(3)$ (namely, a special orthogonal matrix). Such rotation matrix is defined to be the one that aligns the spacecraft-fixed reference frame $\mathcal{F}_{\mathrm{C}}$ to either the inertial reference frame $\mathcal{F}_{\mathrm{I}}$ or to the station-fixed reference frame $\mathcal{F}_{\mathrm{S}}$, depending on what is the current maneuver being described. The equations of motion may be derived in a standard minimal-action variational setting which leads to classical Euler-Poincaré equations. Since the spacecraft is subjected to non-conservative torques, such equations are not 'pure' [29].

The rotational dynamics of a rigid body is expressed by a system of two first-order differential equations [10]:

$$\begin{cases} \dot{R} = R\Omega, \ R(0) = R_0 \\ \mathbb{J}\dot{\Omega} = \mathbb{Q}\Omega + T_{\mathrm{rw}} + T_{\mathrm{rd}}, \ \Omega(0) = \Omega_0 \end{cases} \tag{2.4}$$

where $\dot{R} \in T_R\mathrm{SO}(3)$ denotes the rotational speed-matrix of the spacecraft, $\Omega \in \mathfrak{so}(3)$ denotes the skew-symmetric angular speed-matrix of the spacecraft, the symbol $\mathbb{J} : \mathfrak{so}(3) \to \mathfrak{so}(3)$ denotes the inertia operator, the operator $\mathbb{Q} : \mathfrak{so}(3) \to \mathfrak{so}(3)$ denotes the resultant of inherent torques due to inertia and mass unbalance within the spacecraft, $T_{\mathrm{rw}} \in \mathfrak{so}(3)$ denotes the mechanical torque exerted by the reaction wheels and $T_{\mathrm{rd}} \in \mathfrak{so}(3)$ denotes a random disturbance term.

The operator $\mathbb{J}$, which is not a matrix, and the operator $\mathbb{Q}$ stem from the Euler-Poincaré equations of motion on the Lie group $\mathrm{SO}(3)$. It is assumed here that the inertia tensor of the spacecraft is constant. The function $\mathbb{J}\Omega$ is hence linear (and invertible) in Ω, while the function $\mathbb{Q}\Omega$ is quadratic. As it is clarified in Chapter 3, it is not necessary to specify the structure of the operator $\mathbb{Q}$, since a fully actuated system may be controlled under the principle of dynamics replacement [25], based on inherent dynamics deletion. In the model (2.4), the second equation establishes the rotational speed in the reference frame $\mathcal{F}_{\mathrm{C}}$. The mechanical torque field T_{rw} depends on the actual attitude R through the chosen control law. The first equation in the system (2.4), often referred to as 'reconstruction equation', allows one to reconstruct the actual attitude of the spacecraft in the chosen reference frame.

Remarking that, in the present thesis, the rotation matrix R is the only quantity that is introduced to represent the attitude of a spacecraft, nor quaternions nor Euler nor Tait-Bryan angles are introduced. In addition, the matrix R is always treated as a whole, without any needs to resort to its entries or angular coordinates.

The mass of a spacecraft changes over time due to propellant consumption during rendezvous. Since the total mass m enters the equations of dynamics (2.1), mass decay needs to be taken into account. Mass decay is described through the differential equation [30]:

$$\dot{m} = -\frac{n\bar{f}_{\mathrm{rt}}}{gI_{\mathrm{sp}}},\ m(0) = m_0 \tag{2.5}$$

In the above expression, the constant scalar $\bar{f}_{\mathrm{rt}} > 0$ denotes the maximum thrust of each atlatl, the symbol g denotes the gravitational acceleration, the constant I_{sp} denotes the specific impulse of each atlatl. (Specific impulse is a measure of how efficiently a reaction mass engine creates thrust.) The variable n denotes the number of active thrusters at a given time and may take only the values 0, 2, 4, 6.

Mass distribution also affects the rotational inertia of a spacecraft. However, it is assumed that the contribution of the propellant mass to the total inertia is negligible, hence the inertia tensor is considered constant throughout this document.

2.3 Numerical implementation of the equations of motion

All in one, the system (2.4) constitute a system of differential equations on the tangent bundle $T\mathrm{SO}(3)$, while the Clohessy–Wiltshire model is a system of differential equations in $\mathbb{R}^3$.

The Clohessy–Wiltshire model may be implemented numerically by the help of a forward Euler numerical scheme. Let the discrete-time counterparts of the position vector as p_s, of the linear velocity $v := \dot{p}$ as v_s, of the resultant of all forces $f := f_{\mathrm{rt}} + f_{\mathrm{cc}} + f_{\mathrm{vd}} + f_{\mathrm{rd}}$ as f_s, and of the mass as m_s, where s denotes the step counter. Denoting by h the numerical time-step, the numerical scheme then reads

$$\begin{cases} v_{s+1} = v_s + hf_s/m_s \\ p_{s+1} = p_s + h\,v_s \end{cases} \tag{2.6}$$

The result of such iteration is a numerical approximation of the actual trajectory, namely the quantity p_s approximates the actual coordinate vector $p(hs)$. It is worth noting that, in an ideal setting, the orbital translational motion happens on the $x - z$ plane, hence the coordinate y does not play any role in the model.

Similarly, upon denoting by n_s the discrete-time counterparts of the number of active

thrusters, the equation (2.5) may be solved numerically as

$$m_{s+1} = m_s - \frac{n_s h \bar{f}_{\mathrm{rt}}}{g I_{\mathrm{sp}}} \tag{2.7}$$

To what concerns the numerical integration of the equations (2.4), it pays to introduce discrete-time counterparts of the involved variables, namely R_s for the attitude matrix, Ω_s for the angular speed matrix, and T_s for the resultant torque matrix $T := T_{\mathrm{rw}} + T_{\mathrm{rd}}$. Then the rotational model (2.4) may be simulated numerically by the following iteration

$$\begin{cases} R_{s+1} = R_s \mathrm{Exp}(h\,\Omega_s) \\ \Omega_{s+1} = \Omega_s + h\,\mathbb{J}^{-1}(\mathbb{Q}\Omega_s + T_s) \end{cases} \tag{2.8}$$

Notice briefly that the first iteration rule stems from the theory of numerical integration of differential equations on Lie-group bundles. In the above relations, the symbol Exp denotes matrix exponential. More details can be found in the papers [10, 25].

Chapter 3

Reorientation under directional constraints

The first control problem to be treated is reorientation in the presence of directional constraints. Reorientation consists in generating a control action that changes the attitude of the spacecraft from an initial attitude, represented by a rotation matrix $R_{\mathrm{i}} \in \mathrm{SO}(3)$, to a desired attitude, represented by a rotation matrix $R_{\mathrm{d}} \in \mathrm{SO}(3)$. Without any further constraints, the problem would be solved by the *geodesic* motion (namely, the shortest path in the space $\mathrm{SO}(3)$) from R_{i} to R_{d}. In actual space missions, however, reorientation must take into account directional constraints, which may be classified as

- *mandatory directions*, specified by unit vectors $e_{\mathrm{M},i} \in \mathbb{R}^3$ and angular amplitudes $\theta_{\mathrm{M},i}$, that represent cones of amplitude $\theta_{\mathrm{M},i}$ around given directions $e_{\mathrm{M},i} \in \mathbb{R}^3$, where one of the axis of the spacecraft must always lie within,
- *forbidden directions*, specified by unit vectors $e_{\mathrm{F},i} \in \mathbb{R}^3$ and angular amplitudes $\theta_{\mathrm{F},i}$, that represent cones of amplitude $\theta_{\mathrm{F},i}$ around given directions $e_{\mathrm{F},i} \in \mathbb{R}^3$, where one of the axis of the spacecraft must always keep out from.

The angles $\theta_{\mathrm{M},i}$ are generally wider than the angles $\theta_{\mathrm{F},j}$. An example of mandatory-type constraint arises from the requirement that the boresight of the onboard antenna keeps within the cone of contact of a ground-station antenna. An example of forbidden-type constraint arises from the necessity to make the boresight of a light-sensitive telescope avoid sunbeams and other brights sources.

The directions $e_{\mathrm{M},i}$ and $e_{\mathrm{F},i}$ are generally specified in the inertial reference frame $\mathcal{F}_{\mathrm{I}}$, while the boresight axes of the antenna, hereafter denoted as e_{BA}, and of the sensor, hereafter denoted as e_{BS}, aboard the spacecraft are specified in the spacecraft-fixed reference frame $\mathcal{F}_{\mathrm{C}}$.

Reorientation is effected via virtual potential functions based on the above information. The virtual potential functions defined in the following are based on both an attractive term and

on barrier-type repulsive terms and enter the equations of dynamics through their Riemannian gradient.

3.1 Rotational dynamics control by dynamics replacement and a virtual-attractive-repulsive potential

The aim of control design for reorientation purpose is to determine an appropriate control action that affects the rotational dynamics of the spacecraft through equations (2.4).

In the present thesis, the reaction-wheel torque-type control field is taken as

$$T_{\mathrm{rw}} := -\mathbb{Q}\Omega - K_{\mathrm{f}}\,\Omega - R^{\top}\nabla_R V \tag{3.1}$$

where $V : \mathrm{SO}(3) \to \mathbb{R}$ denotes a virtual attractive-repulsive potential and ∇_R denotes the Riemannian gradient at $R \in \mathrm{SO}(3)$ corresponding to the canonical inner product in the tangent bundle $T\mathrm{SO}(3)$.

The first term on the right-hand side of the relation (3.1) stems from the principle of dynamics replacement. The purpose of such form of cancellation is to overrule the internal dynamics of a rigid body with the aim of replacing it with a desired dynamics. Such principle may also be referred to as *decoupling* [31].

The second term introduces a sort of rotational braking effect, whose purpose is to slow down the rotational motion and make the effective control torque less sensitive to excessive control actions. This term, discussed in [25, 5, 24], also prevents the control algorithm to oscillate excessively around the optimal solution, which is a well-known effect in gradient-based optimization. The constant $K_{\mathrm{f}} > 0$ determines the relative importance of such term. In general, dissipative forces proportional to speed are added to promote asymptotic stabilization of a dynamical system [31].

The third term on the right-hand side of the relation (3.1) provides a torque that drives the attitude of the rigid body toward the minimum of the potential function V. The potential function must be cautiously crafted in such a way to effectively drive the spacecraft from the initial attitude to the desired attitude while avoiding undesired (forbidden) direction and yet meeting favorable (mandatory) inclination. Notice that the potential is defined in the inertial reference frame $\mathcal{F}_{\mathrm{I}}$, and so is its Riemannian gradient $\nabla_R V$, hence it needs to be brought back to the spacecraft-fixed reference frame $\mathcal{F}_{\mathrm{C}}$ before entering the equations by a pre-multiplication by the $\mathcal{F}_{\mathrm{I}}$-to-$\mathcal{F}_{\mathrm{C}}$ reference conversion matrix $R^{\top}$.

On the basis of the chosen control law (3.1), the angular acceleration of the spacecraft reads

$$\mathbb{J}^{-1}(\mathbb{Q}\Omega + T) = \mathbb{J}^{-1}(-K_{\mathrm{f}}\,\Omega - R^{\top}\nabla_R V + T_{\mathrm{rd}}) \tag{3.2}$$

hence, it does not depend on the internal dynamics anymore. According to literature, the inertia matrix of a spacecraft may be taken diagonal (by an appropriate choice of coordinate system $\mathcal{F}_{\mathrm{C}}$) and even isotropic [2, 7]. For the sake of simplification, it is assumed that the three eigenvalues of such matrix take the same value $J_{\mathrm{C}} > 0$, which readily implies that $\mathbb{J}\Omega = J_{\mathrm{C}}\Omega$.

3.2 Additive potential function and related gradient

As a first attempt to define a potential function, based on additive-repulsive potential theory developed in [25, 7, 1], the following expression is taken

$$V_{\mathrm{ADD}}(R) := A(R) + \sum_i B_i(R) \tag{3.3}$$

where $A : \mathrm{SO}(3) \to \mathbb{R}$ denotes an attractive potential, whose purpose is to attract the attitude of the spacecraft toward the desired attitude R_{d}, while each $B_i : \mathrm{SO}(3) \to \mathbb{R}$ is a barrier-type repulsive potential aimed at making the spacecraft avoiding the forbidden direction while keeping up with the mandatory directions.

In order to specify the structure of the attractive term, it is necessary to recall the notion of geodesic distance in $\mathrm{SO}(3)$. Given two attitudes $R_1, R_2 \in \mathrm{SO}(3)$, their geodesic distance is defined as

$$d(R_1, R_2) := \|\mathrm{Log}(R_1^\top R_2)\|_{\mathrm{F}} \tag{3.4}$$

where Log denotes the principal matrix logarithm and the symbol $\|\cdot\|_{\mathrm{F}}$ denotes a Frobenius matrix norm.

Now, the attractive potential is defined as an upside-down bell-shaped function of the geodesic distance between the current attitude and the desired attitude as

$$A(R) := -\tfrac{1}{2} K_{\mathrm{A}} \ell^2 \exp\left(-\frac{d^2(R_{\mathrm{d}}, R)}{\ell^2}\right) \tag{3.5}$$

which appears to be a monotonically increasing function with a minimum in $R = R_{\mathrm{d}}$. The constant $K_{\mathrm{A}} > 0$ determines the absolute strength of this component of the torque, while the constant $\ell > 0$ represents the radius of influence of the potential over the space $\mathrm{SO}(3)$: the larger ℓ, the larger its influence area is.

In order to compute the Riemannian gradient of the attractive potential component, it is worth recalling the golden formula (manifold calculus in system theory and control is described in [32, 33]):

$$\nabla_R d^2(R_{\mathrm{d}}, R) = 2R\mathrm{Log}(R_{\mathrm{d}}^\top R) \tag{3.6}$$

Henceforth is taken the torque term corresponding to the attractive potential as

$$-R^{\top}\nabla_R A = -K_{\mathrm{A}} \exp\left(-\frac{d^2(R_{\mathrm{d}}, R)}{\ell^2}\right) \mathrm{Log}(R_{\mathrm{d}}^{\top} R) \tag{3.7}$$

The repulsive component of the potential is designed to be of barrier type. In the present endeavor, barriers are designed to either keep a given axis of the spacecraft away from forbidden directions or in the angular proximity of mandatory direction.

Given a mandatory direction $e_{\mathrm{M}} \in \mathbb{R}^3$ expressed in the reference system $\mathcal{F}_{\mathrm{I}}$ and an axis of the spacecraft $e_{\mathrm{BA}} \in \mathbb{R}^3$ expressed in the reference system $\mathcal{F}_{\mathrm{C}}$, the cosine of the angle between these two directions is given by $e_{\mathrm{M}}^{\top} R\, e_{\mathrm{BA}}$, where R denotes the current attitude of the spacecraft with respect to the inertial reference system. In order to make sure that the axis e_{BA} keeps at an angular distance from the mandatory direction e_{M} lesser than a prescribed threshold θ_{M}, the following constraint needs to be imposed

$$e_{\mathrm{M}}^{\top} R\, e_{\mathrm{BA}} - \cos\theta_{\mathrm{M}} > 0 \tag{3.8}$$

Such constraint appears as a *linear inequality* in the attitude matrix R.

A barrier potential to secure adherence to such directional constraint reads

$$B_{\mathrm{M}}(R) := -K_{\mathrm{M}} \log(e_{\mathrm{M}}^{\top} R\, e_{\mathrm{BA}} - \cos\theta_{\mathrm{M}}) \tag{3.9}$$

where $K_{\mathrm{M}} > 0$ determines the strength of the corresponding torque term in the control action, while $\log$ denotes natural logarithm. It is immediate to recognize that, as the axis $R\, e_{\mathrm{BA}}$ gets closer to the surface of the mandatory cone, hence the difference $e_{\mathrm{M}}^{\top} R\, e_{\mathrm{BA}} - \cos\theta_{\mathrm{M}}$ approaches 0, the function $B_{\mathrm{M}}(R)$ approaches $+\infty$ hence providing an infinitely steep potential wall (a barrier, in fact).

The above barrier-type virtual potential component is designed to produce an artificial repulsion from the surface of an obstacle, which is represented as the zero sublevel set of a smooth function. The potential component (3.9), albeit formally different, produces the same effect as the virtual potential introduced in [34], which goes to infinity as the inverse of a known scalar-valued analytic function in the close vicinity of an obstacle and decays to zero at some positive level surface sufficiently far from the obstacle. Such approach is, in turn, based on the obstacle-avoidance technique introduced long before in [31] under the acronym FIRAS (Force Inducing an Artificial Repulsion from a Surface).

The function (3.9) may equivalently be written as $B_{\mathrm{M}}(R) := -K_{\mathrm{M}} \log(\mathrm{tr}(R\, e_{\mathrm{BA}} e_{\mathrm{M}}^{\top}) - \cos\theta_{\mathrm{M}})$, where tr denotes matrix trace. Now, in order to compute the Riemannian gradient of

such matrix-to-scalar function, it pays to recall the formula

$$\nabla_R B = R\sigma\left(R^\top \frac{\partial B}{\partial R}\right) \tag{3.10}$$

where $\sigma : \mathbb{R}^{3\times 3} \to \mathfrak{so}(3)$ is a matrix-to-matrix function defines as $\sigma(Y) := \frac{1}{2}(Y - Y^\top)$ that represents an orthogonal projection over the space of skew-symmetric matrices, while the symbol $\frac{\partial}{\partial R}$ denotes the ordinary Jacobian matrix. (It is compelling to specify that the expression (3.10) holds under the assumption that the tangent bundle $T\mathrm{SO}(3)$ is endowed with the canonical inner product $\langle V_1, V_2\rangle_R := \mathrm{tr}(V_1^\top V_2)$ for every $V_1, V_2 \in T_R\mathrm{SO}(3)$.)

In the present case

$$\frac{\partial B_\mathrm{M}}{\partial R} = -\frac{K_\mathrm{M}}{e_\mathrm{M}^\top R\, e_\mathrm{BA} - \cos\theta_\mathrm{M}} e_\mathrm{M} e_\mathrm{BA}^\top \tag{3.11}$$

Therefore, the torque component corresponding to a mandatory-type barrier potential takes the expression

$$-R^\top \nabla_R B_\mathrm{M} = \frac{K_\mathrm{M}}{e_\mathrm{M}^\top R\, e_\mathrm{BA} - \cos\theta_\mathrm{M}} \sigma(R^\top e_\mathrm{M} e_\mathrm{BA}^\top) \tag{3.12}$$

Likewise, given a forbidden direction $e_\mathrm{F} \in \mathbb{R}^3$ expressed in the reference system $\mathcal{F}_\mathrm{I}$ and an axis of the spacecraft $e_\mathrm{BS} \in \mathbb{R}^3$ expressed in the reference system $\mathcal{F}_\mathrm{C}$, the cosine of the angle between these two directions is given by $e_\mathrm{F}^\top R\, e_\mathrm{BS}$. In order to make sure that the axis e_BS keeps at an angular distance from the mandatory direction e_F larger than a prescribed threshold θ_F, the following constraint needs to be imposed

$$\cos\theta_\mathrm{F} - e_\mathrm{F}^\top R\, e_\mathrm{BS} > 0 \tag{3.13}$$

(For comparison purpose is recalled, e.g. from [5], that such constraint written on the basis of a quaternion $[q^\top\ q_0]^\top$ would read

$$\cos\theta_\mathrm{F} - (q_0^2 - q^\top q) e_\mathrm{F}^\top e_\mathrm{BS} - 2 e_\mathrm{F}^\top q q^\top e_\mathrm{BS} - 2 e_\mathrm{F}^\top q_0 q^\times e_\mathrm{BS} > 0$$

where q_0 denotes the real part of the quaternion and the operator $(\cdot)^\times$ returns a $\mathfrak{so}(3)$ matrix from a $\mathbb{R}^3$ vector. Notice that the Jet Propulsion Laboratory (JPL) convention is used to denote quaternions as is customary in the aerospace domain.)

A barrier potential to secure adherence to such directional constraint reads

$$B_\mathrm{F}(R) := -K_\mathrm{F} \log(\cos\theta_\mathrm{F} - \mathrm{tr}(R\, e_\mathrm{BS} e_\mathrm{F}^\top)) \tag{3.14}$$

where $K_\mathrm{F} > 0$ determines the strength of the corresponding torque term in the control action. The torque component corresponding to such a forbidden-type barrier potential takes the

expression

$$-R^\top \nabla_R B_{\mathrm{F}} = \frac{K_{\mathrm{F}}}{e_{\mathrm{M}}^\top R\, e_{\mathrm{BS}} - \cos\theta_{\mathrm{F}}} \sigma(R^\top e_{\mathrm{F}} e_{\mathrm{BS}}^\top) \tag{3.15}$$

Gluing all pieces together, the complete additive potential expression reads

$$\begin{aligned} V_{\mathrm{ADD}}(R) = &-\frac{1}{2} K_{\mathrm{A}} \ell^2 \exp\left(-\frac{d^2(R_{\mathrm{d}}, R)}{\ell^2}\right) - K_{\mathrm{M}} \sum_i \log(e_{\mathrm{M},i}^\top R\, e_{\mathrm{BA}} - \cos\theta_{\mathrm{M},i}) \\ &- K_{\mathrm{F}} \sum_i \log(\cos\theta_{\mathrm{F},i} - e_{\mathrm{F},i}^\top R\, e_{\mathrm{BS}}) \end{aligned} \tag{3.16}$$

The corresponding control torque term $T_{\mathrm{ADD}}(R) := -R^\top \nabla_R V_{\mathrm{ADD}}(R)$ reads

$$\begin{aligned} T_{\mathrm{ADD}}(R) = &-K_{\mathrm{A}} \exp\left(-\frac{d^2(R_{\mathrm{d}}, R)}{\ell^2}\right) \mathrm{Log}(R_{\mathrm{d}}^\top R) + \sum_i \frac{K_{\mathrm{M}}}{e_{\mathrm{M},i}^\top R\, e_{\mathrm{BA}} - \cos\theta_{\mathrm{M},i}} \sigma(R^\top e_{\mathrm{M},i} e_{\mathrm{BA}}^\top) \\ &+ \sum_i \frac{K_{\mathrm{F}}}{e_{\mathrm{F},i}^\top R\, e_{\mathrm{BS}} - \cos\theta_{\mathrm{F},i}} \sigma(R^\top e_{\mathrm{F},i} e_{\mathrm{BS}}^\top) \end{aligned} \tag{3.17}$$

where summations run over the number of mandatory/forbidden constraints, respectively. It is decided to weight the mandatory terms with the same constant K_{M} and all forbidden terms with the same constant K_{F}, although, in practice, every coefficient may be chosen to take a different value.

It is interesting, and perhaps counter-intuitive, to notice that the torques corresponding to mandatory-type constraints look alike the terms corresponding to forbidden-type constraints. However, the scalar coefficients in the former types of constraints are positive-valued, while the coefficients in the latter types are negative-valued, hence they behave in an opposite way.

An important aspect to evaluate is the expression of the potential function $\bar{V}_{\mathrm{ADD}}$ and of the corresponding gradient-based torque component $\bar{T}_{\mathrm{ADD}} = -R_{\mathrm{d}}^\top [\nabla_R V_{\mathrm{ADD}}]_{R=R_{\mathrm{d}}}$ at the expected equilibrium point. Calculations show that

$$\begin{cases} \bar{V}_{\mathrm{ADD}} = -\frac{1}{2} K_{\mathrm{A}} \ell^2 - K_{\mathrm{M}} \sum_i \log(e_{\mathrm{M},i}^\top R_{\mathrm{d}}\, e_{\mathrm{BA}} - \cos\theta_{\mathrm{M},i}) - K_{\mathrm{F}} \sum_i \log(\cos\theta_{\mathrm{F},i} - e_{\mathrm{F},i}^\top R_{\mathrm{d}}\, e_{\mathrm{BS}}) \\ \bar{T}_{\mathrm{ADD}} = \sum_i \frac{K_{\mathrm{M}}}{e_{\mathrm{M},i}^\top R_{\mathrm{d}} e_{\mathrm{BA}} - \cos\theta_{\mathrm{M},i}} \sigma(R_{\mathrm{d}}^\top e_{\mathrm{M},i} e_{\mathrm{BA}}^\top) + \sum_i \frac{K_{\mathrm{F}}}{\cos\theta_{\mathrm{F},i} - e_{\mathrm{F},i}^\top R_{\mathrm{d}} e_{\mathrm{BS}}} \sigma(R_{\mathrm{d}}^\top e_{\mathrm{F},i} e_{\mathrm{BS}}^\top) \end{cases} \tag{3.18}$$

since $d(R_{\mathrm{d}}, R_{\mathrm{d}}) = 0$ and $\mathrm{Log}(R_{\mathrm{d}}^\top R_{\mathrm{d}}) = 0$. The expression $\bar{V}_{\mathrm{ADD}}$ is useful in numerical simulation to verify whether the gradient-based control algorithm seeks in fact the minimum of the potential function.

The expression $\bar{T}_{\mathrm{ADD}}$ tells that even at the equilibrium point exists a non-zero torque that tend to orient the spacecraft in a direction that is not exactly the desired one. In formal terms, the

solution of the equation $T_{\mathrm{ADD}}(R) = 0$ differs from $R = R_{\mathrm{d}}$ because of the residual pull-push effect of the barriers. This effect is not necessarily disruptive for at least two reasons: 1) during reorientation, even if the boresight of a telescope does not match exactly the preferred direction of observation of a target, an observation mission might still be carried out; 2) during docking, a tolerance in the alignment might be borne [35] (as in underwater missions [36]).

With the aim of fixing the above-noted inconsistency, in the next section is presented an alternative control strategy.

3.3 Mixed multiplicative-additive potential and related gradient

There has been a vast effort in the process of selecting suitable potential functions. While authors agree that each sub-goal needs to be assigned a specific function (one to represent the reorientation goal and one to represent each constraint), existing approaches differ on how to combine such terms to concur in the definition of a virtual potential. To recall a few, the paper [7] suggest a mixed multiplicative/additive potential, where the component associated to re-orientation is multiplied by the sum of the barrier-type components associated to directional obstacles. The paper [5] follows a similar approach, although the components associated to re-orientation and obstacles differ in mathematical structure. The paper [37] remarks that a combination of partial potentials may yield a function with potentially multiple critical points and recall the notion of 'navigation functions' which constitute possible remedies to such difficulty. The function proposed in [37] is a nonlinear combination of the reorientation potential and of the sum of the reorientation-potential with the product of constraint-enforcing potentials.

In the present thesis, it is deemed appropriate to explore the features of a mixed potential inspired by the paper [7]. Such mixed potential is a variant of the additive potential (3.3) and reads

$$V_{\mathrm{MIX}}(R) := A(R) + M(R) \sum_i B_i(R) \tag{3.19}$$

where the barrier functions take the same expression as in (3.9) and (3.14), the attractive function $A(R)$ takes the same expression as in (3.5), while the additive potential is taken as a quadratic function as

$$M(R) := -\tfrac{1}{2} d^2(R, R_{\mathrm{d}}) \tag{3.20}$$

which is a monotonically increasing function with one minimum in $R = R_{\mathrm{d}}$.

The detailed expression of the mixed-form potential reads

$$V_{\mathrm{MIX}}(R) = -\frac{1}{2}K_{\mathrm{A}}\,\ell^2 \exp\left(-\frac{d^2(R,R_{\mathrm{d}})}{\ell^2}\right) - \frac{1}{2}d^2(R,R_{\mathrm{d}})\left(K_{\mathrm{M}}\sum_i \log(e_{\mathrm{M},i}^{\top} R\, e_{\mathrm{BA}} - \cos\theta_{\mathrm{M},i}) + K_{\mathrm{F}}\sum_i \log(\cos\theta_{\mathrm{F},i} - e_{\mathrm{F},i}^{\top} R\, e_{\mathrm{BS}})\right) \tag{3.21}$$

The torque control component corresponding to the Riemannian gradient of such virtual potential may be determined by going through the same calculations shown in Section 3.2. The obtained expression $T_{\mathrm{MIX}}(R) := -R^{\top}\nabla_R V_{\mathrm{MIX}}(R)$ reads

$$\begin{aligned} T_{\mathrm{MIX}} = &-K_{\mathrm{A}}\exp\left(-\frac{d^2(R,R_{\mathrm{d}})}{\ell^2}\right)\mathrm{Log}(R_{\mathrm{d}}^{\top}R) \\ &+\left(K_{\mathrm{M}}\sum_i \log(e_{\mathrm{M},i}^{\top} R\, e_{\mathrm{BA}} - \cos\theta_{\mathrm{M},i}) + K_{\mathrm{F}}\sum_i \log(\cos\theta_{\mathrm{F},i} - e_{\mathrm{F},i}^{\top} R\, e_{\mathrm{BS}})\right)\mathrm{Log}(R_{\mathrm{d}}^{\top}R) \\ &+\frac{1}{2}d^2(R,R_{\mathrm{d}})\left(\sum_i \frac{K_{\mathrm{M}}}{e_{\mathrm{M},i}^{\top} R\, e_{\mathrm{BA}} - \cos\theta_{\mathrm{M},i}}\sigma(R^{\top}e_{\mathrm{M},i}e_{\mathrm{BA}}^{\top}) + \sum_i \frac{K_{\mathrm{F}}}{e_{\mathrm{F},i}^{\top} R\, e_{\mathrm{BS}} - \cos\theta_{\mathrm{F},i}}\sigma(R^{\top}e_{\mathrm{F},i}e_{\mathrm{BS}}^{\top})\right) \end{aligned} \tag{3.22}$$

With reference to the classical error-feedback control, it is worth noticing that in the above expression $E := \mathrm{Log}(R_{\mathrm{d}}^{\top}R)$ represents the reorientation error. It is immediate to recognize that, at the sought equilibrium point $R = R_{\mathrm{d}}$, it holds that $V_{\mathrm{MIX}}(R_{\mathrm{d}}) = 0$ and, more importantly, that $T_{\mathrm{MIX}}(R_{\mathrm{d}}) = 0$. Such approach might potentially be able to overcome the problem of non-zero torque at equilibrium entailed by the approach presented in Section 3.2. The virtual potential (3.21) may be interpreted as an additive repulsive potential weighted by an additive potential increasing with the distance to the desired attitude.

A potential drawback of the mixed multiplicative-additive approach just detailed is that, as opposed to the additive approach explained in Section 3.2, there is no chance to balance, through a weighting constant, the opposed actions of the attractive term and of the repulsive terms.

3.4 Relation with a navigation function

The barrier terms, that the above-discussed virtual potential functions are based on, may be recast in a different expression by exploiting the properties of the logarithm. In fact, upon defining the total barrier term

$$B_{\mathrm{T}} := K_{\mathrm{M}}\sum_i \log(e_{\mathrm{M},i}^{\top} R\, e_{\mathrm{BA}} - \cos\theta_{\mathrm{M},i}) + K_{\mathrm{F}}\sum_i \log(\cos\theta_{\mathrm{F},i} - e_{\mathrm{F},i}^{\top} R\, e_{\mathrm{BS}}) \tag{3.23}$$

it is immediate to recognize that

$$\begin{aligned} B_{\mathrm{T}} &= \sum_i \log(e_{\mathrm{M},i}^{\top} R\, e_{\mathrm{BA}} - \cos\theta_{\mathrm{M},i})^{K_{\mathrm{M}}} + \sum_i \log(\cos\theta_{\mathrm{F},i} - e_{\mathrm{F},i}^{\top} R\, e_{\mathrm{BS}})^{K_{\mathrm{F}}} \\ &= \log\left(\prod_i (e_{\mathrm{M},i}^{\top} R\, e_{\mathrm{BA}} - \cos\theta_{\mathrm{M},i})^{K_{\mathrm{M}}} \prod_i (\cos\theta_{\mathrm{F},i} - e_{\mathrm{F},i}^{\top} R\, e_{\mathrm{BS}})^{K_{\mathrm{F}}} \right) \end{aligned} \tag{3.24}$$

It readily follows that

$$\exp(B_{\mathrm{T}}) = \prod_i \prod_j (e_{\mathrm{M},i}^{\top} R\, e_{\mathrm{BA}} - \cos\theta_{\mathrm{M},i})^{K_{\mathrm{M}}} (\cos\theta_{\mathrm{F},j} - e_{\mathrm{F},j}^{\top} R\, e_{\mathrm{BS}})^{K_{\mathrm{F}}} \tag{3.25}$$

Hence the total barrier function may be regarded as a product of partial function that are positive only in the permissible zones delimited by each barrier, a design strategy suggested in [37], where the weighting coefficients K_{M} and K_{F} play the role of order parameters.

Chapter 4

Position control during cruising and docking under positional constraints

Autonomous navigation toward the space station aimed at complete docking is one of the primary goals of control design. Since navigation is a complex task, it is customary to break it into subtasks [2] to be separately tackled on the basis of the current physical distance between the spacecraft and the docking port. In the present thesis, the approaching trajectory is subdivided in three boats: cruising, far-end docking and near-end docking, as detailed in the next sections.

4.1 Control strategy during cruising in the presence of physical obstacles

The maneuver of a spacecraft requires, in the presence of obstacles, to be carried out autonomously by the help of sensors by a guidance algorithm. The algorithm devised in the present thesis is based on virtual attractive-repulsive potential theory and is declined in three versions: a version adapted from [2], a version based on impulsive control drawn from [1], and a version build on impulsive control by an adaptive desired speed.

During an approaching phase, the motion of the spacecraft is referred to the station's LVLH reference system, hence the attitude matrix R, in the present context, is the one that aligns the spacecraft-fixed reference frame $\mathcal{F}_{\mathrm{C}}$ to the station-fixed reference frame $\mathcal{F}_{\mathrm{S}}$.

According to the work [2], the control algorithm switches on the thrusters according to a first-order sliding-mode control method, described by the relation:

$$f_{\mathrm{rt}} = -2\,\varphi\,\bar{f}_{\mathrm{rt}}\,R\,\mathrm{sign}(\sigma) \tag{4.1}$$

which expresses the fact that a pair of thrusters per axis of the spacecraft is eventually switched on, hence exert a thrust twice as large as the maximum thrust. Which pair of thrusters is currently switched on is determined by the sliding output vector $\sigma \in \mathbb{R}^3$, whose value is inessential except

for the signs of its components. The variable $\varphi \in \{0, 1\}$ represents a flag employed in impulsive control.

In general, sliding mode control (SMC) is based on discontinuous feedback that switches among a number of control laws according to a pre-defined decision rule. For a basic review of its features, readers might consult [38, 39]. For a more advanced account of SMC, interested readers might consult [40].

It is worth highlighting that the force term f_{rt} and the number n are related through the relation

$$\varphi \, \|f_{\mathrm{rt}}\|^2 = 2 \, n \, \bar{f}_{\mathrm{rt}}^2 \tag{4.2}$$

which, in fact, allows determining the number of active thrusters on the basis of the output of the control algorithm.

The variable σ depends on the mismatch between the current velocity $\dot{p}$ of the spacecraft and the desired velocity $\dot{p}_{\mathrm{d}} \in \mathbb{R}^3$, as well as on the mismatch between the current position p of the spacecraft and the desired position $p_{\mathrm{d}} \in \mathbb{R}^3$, through the linear combination

$$\sigma := \dot{p} - \dot{p}_{\mathrm{d}} + c(p - p_{\mathrm{d}}) \tag{4.3}$$

The constant $c \geqslant 0$ determines the relative weight between position and velocity mismatch.

The quantity p_{d} is determined by the position of the target of the cruising phase, which normally is located from within a few hundreds to a few dozen meters away from the docking port, and is generally constant. The desired velocity changes along the trajectory and is determined through a virtual potential by the following expression

$$\dot{p}_{\mathrm{d}} = v_{\mathrm{d}} \frac{-\nabla_p V_{\mathrm{C}}}{\|\nabla_p V_{\mathrm{C}}\|} \tag{4.4}$$

where $v_{\mathrm{d}} > 0$ denotes the desired speed, determined independently of the virtual potential, while $\nabla_p V_{\mathrm{C}} \in \mathbb{R}^3$ denotes the gradient of the potential $V_{\mathrm{C}} : \mathbb{R}^3 \to \mathbb{R}$. As a result, it holds that $\|\dot{p}_{\mathrm{d}}\| = v_{\mathrm{d}}$, hence, the entity and the direction of the desired speed are determined independently by the control algorithm.

The cruising phase ends when the distance between the spacecraft and the desired position is less than a given threshold, namely, as soon as $\|p - p_{\mathrm{d}}\| \geqslant 50$.

4.2 Virtual potential design

The virtual potential function is designed to decrease when a spacecraft gets closer to the target location and to increase when a spacecraft gets closer to a physical obstacle. The gradient-based

sliding-mode control algorithm is hence designed to seek the minimum of the potential function.

The virtual potential is constructed as a sum of terms, one of which is attractive and depends on the desired location, while further terms are repulsive and depend on the location and on the safety radii of physical obstacles. Formally, the potential reads

$$V_{\mathrm{C}}(p) = A_{\mathrm{C}}(p) + \sum_i P_{\mathrm{C},i}(p) \tag{4.5}$$

where $A_{\mathrm{C}} : \mathbb{R}^3 \to \mathbb{R}$ denotes the attractive-type component and $P_{\mathrm{C},i} : \mathbb{R}^3 \to \mathbb{R}$ denote the repulsive-type components. The sum runs over the number of obstacles within the radius of sensitivity of the proximity sensors aboard the spacecraft.

The attractive-type component of the potential function is defined by

$$A_{\mathrm{C}}(p) := \tfrac{1}{2} H_{\mathrm{A}} \|p - p_{\mathrm{d}}\|^2 \tag{4.6}$$

where $H_{\mathrm{A}} > 0$ is a constant that determines the strength of the attractive component of the potential. The component $A_{\mathrm{C}}(p)$ is monotonically increasing with a unique minimum in $p = p_{\mathrm{d}}$.

In order to enable the spacecraft to avoid the physical obstacles, a number of repulsive-type components need to be designed that exhibit their maximum value in correspondence to the location of the obstacles and whose action peter out rapidly as the distance between the spacecraft and the obstacles increases. It is denoted as $o_i \in \mathbb{R}^3$ the location of each obstacle in the station-fixed reference frame $\mathcal{F}_{\mathrm{S}}$ and by η_i the safety radius of each obstacle. Obstacles are assumed to be of spherical shape, hence each safety radius may be thought of as the sum of the radius of the spherical obstacle augmented by an extra safety distance (which should not exceed the sensitivity radius of the proximity sensor). On the basis of such data, the repulsive-type component of the potential associated to the i^{th} obstacle is defined as

$$P_{\mathrm{C},i}(p) := \frac{1}{2} H_{\mathrm{R}} \exp\left(-\frac{\|p - o_i\|^2}{\eta_i^2}\right) \tag{4.7}$$

where the constant $H_{\mathrm{R}} > 0$ determines the strength of each repulsive term. Notice that the expression chosen represents only a soft constraint, although it cannot be ensured that the spacecraft will not enter the obstacles, a reasonable safety distance may be determined through a careful handcrafting of the safety radii.

The anti-gradient of the virtual potential function reads

$$-\nabla_p V_{\mathrm{C}} = -H_{\mathrm{A}}(p - p_{\mathrm{d}}) + H_{\mathrm{R}} \sum_i \exp\left(-\frac{\|p - o_i\|^2}{\eta_i^2}\right) \frac{p - o_i}{\eta_i^2} \tag{4.8}$$

It is important to remark that the present setting stays unvaried whether the obstacles are fixed with respect to the reference frame $\mathcal{F}_{\mathrm{S}}$ or are moving, instead.

4.3 Speed intensity determination

The desired speed may be determined on the basis of different criteria. In the present thesis, the performances of three strategies are compared to determine such speed.

The computationally simplest strategy is drawn from reference [2] and consists in setting the desired speed to the maximum allowable speed $\bar{v}$ and the flag φ to 'on'-state, namely

$$v_{\mathrm{d}} = \bar{v},\ \varphi = 1 \tag{4.9}$$

The next strategy examined is inspired by the notion of impulsive control discussed in [1]. It consists in switching on the reaction thrusters only when the spacecraft effectively gets off the right track, hence keeping them off whenever not necessary, with the aim to save propellant. Formally

$$v_{\mathrm{d}} = \bar{v},\ \varphi = \begin{cases} 1, & \text{if } \Delta\xi > \tau \\ 0, & \text{otherwise} \end{cases} \tag{4.10}$$

where $\Delta\xi := \left\| \frac{\dot{p}}{\|\dot{p}\|} - \frac{\nabla_p V_{\mathrm{C}}}{\|\nabla_p V_{\mathrm{C}}\|} \right\|$ and τ denotes a predefined threshold that determines the sensitivity of the algorithm to difference in direction. It is found empirically that the threshold should be of the order of 10^{-2}. In fact, it is set $\tau = 0.05$. Notice that this strategy only influences the 'off'-state of the thrusters, while it does not influence the 'on'-state.

An allegedly more proficient strategy also influences the 'on'-state of the thrusters by determining the speed amplitude. The law suggested to determine speed is such that the more the spacecraft gets closer to the target, the lesser the cruising speed is. In formulas:

$$\begin{cases} v_{\mathrm{d}} = \min\left\{\bar{v}, 5\Delta\xi\|p - p_{\mathrm{d}}\|^{\frac{1}{4}}\right\} \\ \varphi = \begin{cases} 1, & \text{if } \Delta\xi > \tau \\ 0, & \text{otherwise} \end{cases} \end{cases} \tag{4.11}$$

The relationship to determine the desired speed intensity is empirically handcrafted. The hard-limiting check prevents the computed speed to exceed its maximum allowable value.

4.4 Attitude control during a cruising phase

During cruising, it is not essential to control the attitude of a spacecraft, which may keep a constant orientation resulting from previous maneuvers, until the beginning of the docking phase. This statement can be made provided that the spacecraft has a sufficient number of sensors on board to detect the presence of obstacles whatever the attitude is. Nevertheless, to aid stability of a spacecraft [2] against unforeseen events, in the present thesis, it is deemed it appropriate to explore attitude regulation strategies.

A way to control orientation during cruising is to establish a desired attitude R_{d} and to set up a control strategy to make sure the actual attitude matrix R of the spacecraft adheres to the desired attitude. In order to control the attitude of the spacecraft, a control torque is chosen according to synchronization theory [11] to be

$$T_{\mathrm{rw}} := -\mathbb{Q}\Omega - K_{\mathrm{f}}\,\Omega - K_{\mathrm{S}}\log(R_{\mathrm{d}}^{\top}R) \tag{4.12}$$

where $K_{\mathrm{S}} > 0$ determines the strength of coupling in the leader/follower pair. (Notice that the term $K_{\mathrm{S}}\log(R_{\mathrm{d}}^{\top}R)$ stems as the Riemannian gradient ∇_R of the potential function $\frac{1}{2}K_{\mathrm{S}}\,d^2(R,R_{\mathrm{d}})$ and may be recognized as the 'proportional' component of a Lie-group type PID controller.)

To what concerns the desired attitude, two possibilities are explored. A first attempt consists in setting up a fixed attitude matrix that coincides with the one required for docking, namely $R_{\mathrm{d}} = I_3$. As a second attempt, the desired attitude is set up to the one which corresponds to the direction of the desired speed $\dot{p}_{\mathrm{d}}$ as defined in (4.4). The relation between the (time-varying) matrix R_{d} and the components of the desired speed vector $\dot{p}_{\mathrm{d}}$ may be found in [2], in equations (15)-(17).

A third strategy, corresponding to lack of synchronization, is tested against the former two methods. This corresponds to setting the control torque as

$$T_{\mathrm{rw}} := -\mathbb{Q}\Omega - K_{\mathrm{f}}\,\Omega \tag{4.13}$$

which aims at just passivating the spacecraft and to mitigate the effects of unpredictable disturbances.

A fourth strategy, loosely based on [25], consists in setting up a control torque that tends to align the speed $\dot{p}$ of the spacecraft to the desired speed resulting from the virtual potential function described in Section 4.1, namely $-\frac{\nabla_p V_{\mathrm{C}}}{\|\nabla_p V_{\mathrm{C}}\|}$. The corresponding torque term reads

$$T_{\mathrm{rw}} := -\mathbb{Q}\Omega - K_{\mathrm{f}}\,\Omega + \frac{K_{\mathrm{FBP}}}{\|\nabla_p V_{\mathrm{C}}\|}(\dot{p}(\nabla_p V_{\mathrm{C}})^{\top} - (\nabla_p V_{\mathrm{C}})\dot{p}^{\top}) \tag{4.14}$$

where $K_{\mathrm{FBP}} > 0$ denotes the aligning torque. Notice that the rightmost terms corresponds to the cross product $\dot{p} \wedge (\nabla_p V_{\mathrm{C}})$ in $\mathfrak{so}(3)$, which vanishes when these vectors are parallel.

4.5 Final guidance to docking in the absence of physical obstacles

In close proximity to the space station, at a distance of a few dozen meters, it is reasonable and safe to assume that no large obstacles stand in the way to the space station. During the final approach maneuver, therefore, the only obstacle to be taken into account is the outer structure of the space station itself.

In order to avoid colliding with any part of the station, a technique adapted from [1] is deployed, based on a safety zone whose border takes the shape of a cardioid curve. The radius of the cardioid must be selected in such a way to encompass the whole space station in order to allow a spacecraft to safely approach from every direction. The cardioid itself includes a recess, a cuspid whose tip coincides with the docking port and whose asymptote coincides with the docking axes (taken to be the X axis of the LVLH reference frame). The actual maneuver during docking is divided into two subtasks.

The first subtask is termed *far-end approaching*. It ensures that, no matter what is the direction of arrival of the spacecraft, it gets positioned to the right of the docking port while avoiding the outskirts of the space station by keeping out of the cardioid-shaped safety region. This procedure takes, as input, the desired location $p_{\mathrm{fe}} \in \mathbb{R}^3$ for this intermediate step and the safety radius of the space station, that shall be denoted as r_{S}. The tip of the cardioid cusp is located at $p_{\mathrm{fe}} \in \mathbb{R}^3$ and the cusp opens along the X axis. The far-end approaching phase continues until the distance between the spacecraft and the desired position is less than a given threshold, namely, as soon as $\|p - p_{\mathrm{fe}}\| \geqslant 1$.

The current distance and angle of arrival, in the LVLH reference frame $\mathcal{F}_{\mathrm{S}}$, are calculated as

$$\begin{cases} \rho = \|p - p_{\mathrm{fe}}\| \\ \theta = \frac{\pi}{2} - \operatorname{atan2}((p - p_{\mathrm{fe}})^{\top} e_{\mathrm{x}}, -(p - p_{\mathrm{fe}})^{\top} e_{\mathrm{z}}) \end{cases} \tag{4.15}$$

where the function $\operatorname{atan2}(\cdot)$ returns the correct and unambiguous value for the angle while converting from Cartesian coordinates to polar coordinates.

The cardioid is built from its parametric equations and a preferred direction is evaluated at each position during the far-end phase from the boundary tangent vector of the cardioid

$$\gamma_{\mathrm{fe}} = \begin{cases} \dot{x} = -H_{\mathrm{t}}(\sin(\theta) - \sin(2\theta)) \\ \dot{y} = 0 \\ \dot{z} = -H_{\mathrm{t}}(\cos(\theta) - \cos(2\theta)) \end{cases} \tag{4.16}$$

where $H_{\mathrm{t}} > 0$.

The control strategy used is a variable desired speed control similar to the one described from the cruising phase

$$\begin{cases} v_{\mathrm{d}} = \min\left\{\bar{v}_{\mathrm{fe}}, \Delta\xi\rho^{\frac{1}{4}}\right\} \\ \varphi = \begin{cases} 1, & \text{if } \Delta\xi > \tau \\ 0, & \text{otherwise} \end{cases} \end{cases} \tag{4.17}$$

where $\Delta\xi := \left\| \frac{\dot{p}}{\|\dot{p}\|} - \frac{\gamma_{\mathrm{fe}}}{\|\gamma_{\mathrm{fe}}\|} \right\|$ and $\bar{v}_{\mathrm{fe}} = \frac{\bar{v}}{10}$, the expression of $\bar{v}_{\mathrm{fe}}$ is chosen empirically after evaluating some real cases of docking maneuvers.

The second subtask is termed *near-end approaching*, it ensures slow and steady docking in the absence of any obstacle of sort, except for the docking port. Such procedure takes, as input, the desired location $p_{\mathrm{ne}} \in \mathbb{R}^3$ to drive the spacecraft to the docking port. Since the spacecraft is now aligned with the docking axis, the preferred direction is defined as

$$\gamma_{\mathrm{ne}} = -e_{\mathrm{x}} \tag{4.18}$$

during the all phase.

The control strategy used in this phase is a variable desired speed control as described before but considering instead a non-impulsive control, this choice depends on the necessity to have the best level of precision possible. Respect than the previous phases, it can be easily understood this requirement in proximity of the docking port. In formulas:

$$v_{\mathrm{d}} = \min\{\bar{v}_{\mathrm{ne}}, \Delta\xi\rho^{\frac{1}{4}}\} \tag{4.19}$$

where $\Delta\xi := \left\| \frac{\dot{p}}{\|\dot{p}\|} - \frac{\gamma_{\mathrm{ne}}}{\|\gamma_{\mathrm{ne}}\|} \right\|$, $\rho := \|p - p_{\mathrm{ne}}\|$ and $\bar{v}_{\mathrm{ne}} = \bar{v}_{\mathrm{fe}}$.

The near-end approaching phase continues until the distance between the spacecraft and the desired position is ideally zero, especially considering the position p of the spacecraft as the position of its center of mass, the end of this phase comes when that distance is equal to the one between the center of mass and the juncture port of the spacecraft.

4.6 Alignment to a docking axis during final guidance

In order to regulate the attitude of a spacecraft during the final guidance stage, a control torque is again chosen according to synchronization to be

$$T_{\mathrm{rw}} := -\mathbb{Q}\Omega - K_{\mathrm{f}}\,\Omega - K_{\mathrm{D}}\log(R_{\mathrm{d}}^{\top}R) \tag{4.20}$$

with $K_{\mathrm{D}} > 0$.

During final guidance, the desired attitude of the spacecraft is constant to $R_{\mathrm{d}} = I_3$, which describes a state of stable alignment between the reference system $\mathcal{F}_{\mathrm{C}}$ and the frame $\mathcal{F}_{\mathrm{S}}$. Hence, the expression of the active torque may be simplified to $T_{\mathrm{rw}} = -\mathbb{Q}\Omega - K_{\mathrm{f}}\,\Omega - K_{\mathrm{D}}\log(R)$.

Chapter 5

Results of numerical experiments

The parameters that appear in the mathematical model of a spacecraft motion are summarized in Table 5.1.

Parameter	Symbol	Value
Initial spacecraft mass	m_0	600 (kg)
Maximum allowable speed	$\bar{v}$	6 (m/s)
Principal inertia	J_{C}	144 (kg·m^2)
Maximum thrust	$\bar{f}_{\mathrm{rt}}$	10 (N)
Frontal area	S	1.44 (m^2)
Drag coefficient	C_{D}	2.20 $(-)$
Specific impulse	I_{sp}	220 (s)
Gravitational acceleration	g	9.81 (m/s^2)
Atmosphere density	ρ	10^{-12} (kg/m^3)
Orbit radius	r	$6,878 \cdot 10^3$ (m)
Gravitational parameter	μ	$3.986 \cdot 10^{14}$ (m^3/s^2)

Table 5.1: Physical parameters and constants entering the spacecraft model.

5.1 Numerical simulations on reorientation

In order to test the reorientation strategy, numerical experiments adapted from [7] are performed. Simulations come with two different potentials, namely additive-potential and mixed-potential. Since it occurred to detect some inconsistencies in the numerical data, some data are adapted to restore consistency.

In these experiments, the spacecraft is assumed to be endowed with a radio antenna whose boresight axis is $e_{\mathrm{BA}} = e_{\mathrm{y}}$ and a sensor whose boresight axis is $e_{\mathrm{BS}} = e_{\mathrm{z}}$. In order to evaluate the performance of reorientation, the following figure of merit, referred to as Reorientation

Performance Indicator, is defined:

$$\mathrm{RPI} := 100\left(1 - \frac{d(R_\mathrm{a}, R_\mathrm{d})}{d(R_\mathrm{i}, R_\mathrm{d})}\right)\ (\%) \tag{5.1}$$

where R_a denotes the attitude actually achieved by the reorientation control algorithm in the given time frame. All experiments in the present section are performed with a stepsize $h = 0.01$ (sec).

In the following experiments, the initial angular speed Ω_0 is set to 0_3 (which denotes a null 3×3 matrix).

5.1.1 Experiment 1

The first experiment consisted in simulating reorientation from an initial attitude, described by the matrix R_i to a desired attitude, described by the rotation matrix R_d, in the presence of a mandatory zone, according to *Case 2* discussed in the paper [7].

The problem is tackled by an additive-potential-based control algorithm as explained in Section 3.2. In this experiment, the potential and the associated torque read

$$\begin{cases} V_\mathrm{ADD}(R) = & -\frac{1}{2}K_\mathrm{A}\ell^2 \exp\left(-\frac{d^2(R_\mathrm{d},R)}{\ell^2}\right) - K_\mathrm{M}\log(e_\mathrm{M}^\top R\, e_\mathrm{BA} - \cos\theta_\mathrm{M}) \\ T_\mathrm{ADD}(R) = & -K_\mathrm{A}\exp\left(-\frac{d^2(R_\mathrm{d},R)}{\ell^2}\right)\mathrm{Log}(R_\mathrm{d}^\top R) + \frac{K_\mathrm{M}}{e_\mathrm{M}^\top R\, e_\mathrm{BA} - \cos\theta_\mathrm{M}}\sigma(R^\top e_\mathrm{M}\, e_\mathrm{BA}^\top) \end{cases} \tag{5.2}$$

The Table 5.2 shows the data pertaining to this simulation tackled with a virtual additive potential.

Description	Symbol	Value
Initial attitude	R_i	$\begin{bmatrix} 0.3181 & 0.9375 & -0.1409 \\ 0.7050 & -0.3333 & -0.6260 \\ 0.6339 & -0.0998 & 0.7670 \end{bmatrix}$
Desired attitude	R_d	$\begin{bmatrix} 0.0265 & 0.7821 & 0.6226 \\ 0.2073 & 0.6050 & -0.7688 \\ 0.9779 & -0.1494 & 0.1462 \end{bmatrix}$
Mandatory direction	e_M	$[0.8530\ -0.2653\ 0.4495]^\top$
Aperture of the mandatory cone	θ_M	70 (°)
Constant K_A	K_A	$2.8 \cdot 10^{-1} J_\mathrm{C}$
Constant ℓ^2	ℓ^2	50
Constant K_f	K_f	$1.4 J_\mathrm{C}$
Constant K_M	K_M	$1 \cdot 10^{-5} J_\mathrm{C}$

Table 5.2: Numerical data corresponding to the numerical Experiment 1 tackled with a virtual additive potential. The initial and desired attitude are represented using a 3×3 *matrix.*

The numerical results obtained with an additive potential are illustrated in the Figure 5.1. The result achieved by the control algorithm in the given time frame is $\mathrm{RPI} = 100\%$ and the trajectory can also be visualized in Figure 5.2.

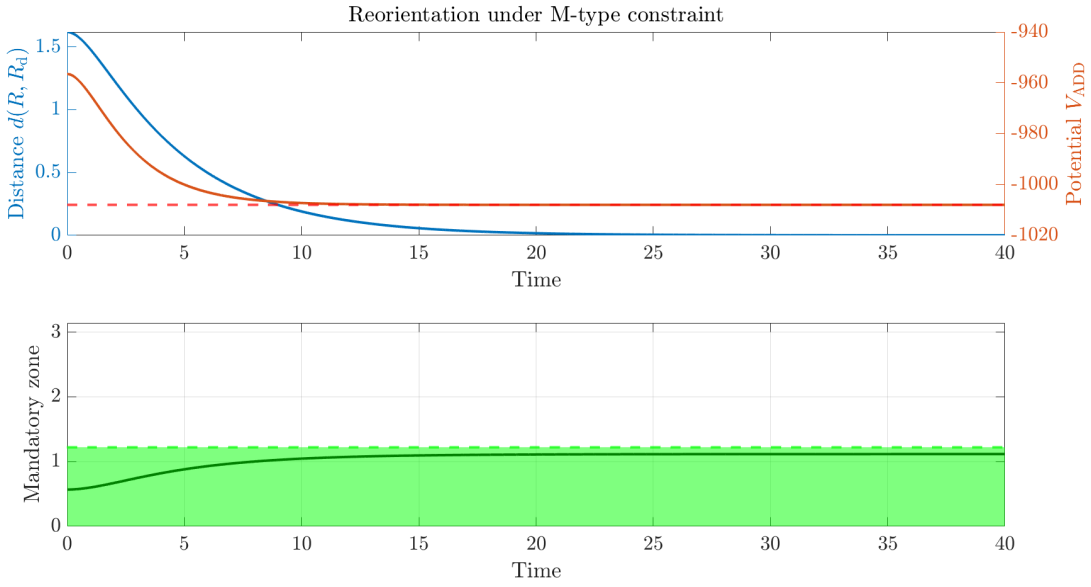

Figure 5.1: Numerical results obtained for the Experiment 1 using additive-potential-based control algorithm. Top panel: values of the distance between the actual attitude and the desired attitude, and value of the potential during reorientation; the dashed line represents the theoretically evaluated minimum value of the potential pertaining to this experiment. Bottom panel: Angle between the boresight direction of the antenna and the mandatory direction; the green area represents the mandatory zone. Time is measured in seconds.

As it may be readily appreciated from the figure, the optimization-based control algorithm effectively attains the minimum value of the potential function while keeping the boresight of the antenna within the mandatory cone. It is interesting to point out that, through some handcrafting of the constants, it is possible to operate while being really close to the barrier and reach the goal.

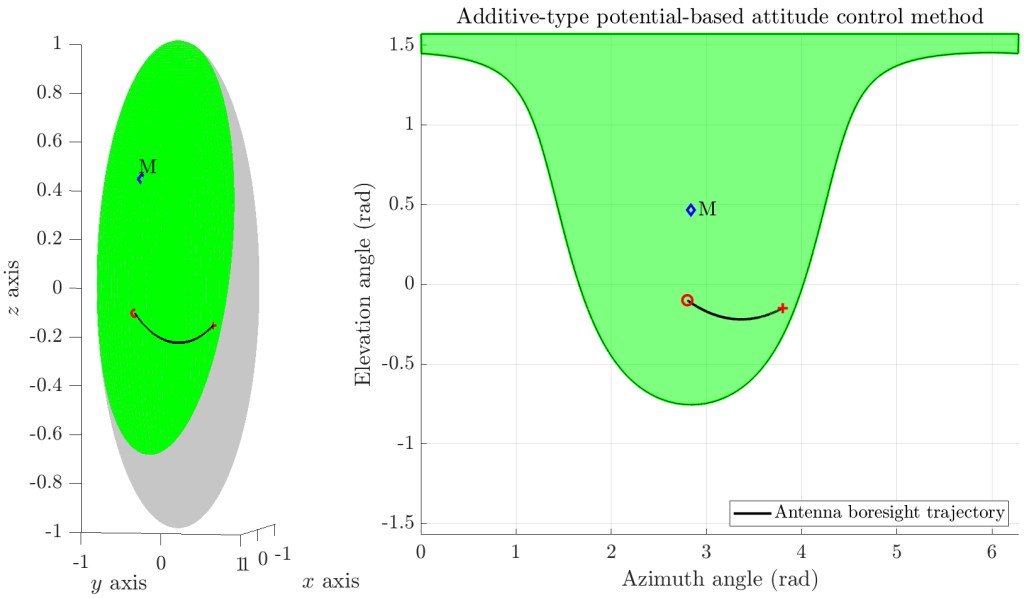

Figure 5.2: Trajectory achieved by the mandatory axis as explained in Experiment 1 using additive-potential-based control algorithm. Left panel: The trajectory is shown on a sphere that surrounds the satellite and centered in the center of gravity of the spacecraft. Right panel: Two-dimensional representation of the sphere, the mandatory zone and the trajectory of the mandatory axis. The red cross represents the attitude reached at the end of the simulation, while the red circle represents the initial attitude.

Now is presented a different approach to the same problem (*Case 2* of the paper [7]) that uses a variant of the previously explained potential-based maneuver, which is the mixed additive-multiplicative potential-based approach explained in Section 3.3. From now on, this approach is referred to as mixed-potential-based control. The potential and the associated torque of this experiment read:

$$\begin{cases} V_{\mathrm{MIX}}(R) = & -\frac{1}{2}K_{\mathrm{A}}\ell^2 \exp\left(-\frac{d^2(R_{\mathrm{d}},R)}{\ell^2}\right) - K_{\mathrm{M}}\frac{d^2(R_{\mathrm{d}},R)}{2}\log(e_{\mathrm{M}}^{\top}R\,e_{\mathrm{BA}} - \cos\theta_{\mathrm{M}}) \\ T_{\mathrm{MIX}}(R) = & -K_{\mathrm{A}}\exp\left(-\frac{d^2(R_{\mathrm{d}},R)}{\ell^2}\right)\mathrm{Log}(R_{\mathrm{d}}^{\top}R) + K_{\mathrm{M}}\log(e_{\mathrm{M}}^{\top}R\,e_{\mathrm{BA}} - \cos\theta_{\mathrm{M}})\mathrm{Log}(R_{\mathrm{d}}^{\top}R) \\ & + \frac{d^2(R_{\mathrm{d}},R)}{2}\frac{K_{\mathrm{M}}}{e_{\mathrm{m}}^{\top}R\,e_{\mathrm{BA}}^{\top} - \cos\theta_{\mathrm{M}}}\,\sigma(R^{\top}\,e_{\mathrm{M}}\,e_{\mathrm{BA}}^{\top}) \end{cases} \tag{5.3}$$

The Table 5.3 shows the data pertaining to this simulation tackled with a virtual mixed potential. The initial and desired attitude are not shown as they are the same as additive potential as well as the mandatory direction and its aperture of mandatory cone.

Description	Value
Constant K_{A}	$9.3 \cdot 10^{-2} J_{\mathrm{C}}$
Constant ℓ^2	50
Constant K_{f}	$1.4 J_{\mathrm{C}}$
Constant K_{M}	$0.1 J_{\mathrm{C}}$

Table 5.3: Numerical data corresponding to the numerical Experiment 1 using mixed additive-multiplicative potential-based control algorithm.

The numerical results obtained with a mixed potential are illustrated in the Figure 5.3. The result achieved by the control algorithm in the given time frame is $\mathrm{RPI} = 100\%$. By comparing the two approaches that tackle the same problem (Figure 5.2 and Figure 5.4), where the former shows the additive potential case while the latter displays the mixed potential case, it can be noticed that the trajectories are not exactly the same but really similar to each other. This is, in fact, a particular case in which the constraint for the attitude is only to stay inside the mandatory zone, hence the trajectories are really close to the fastest way to get to the desired attitude and will only differ slightly when handcrafting the constants in the algorithm.

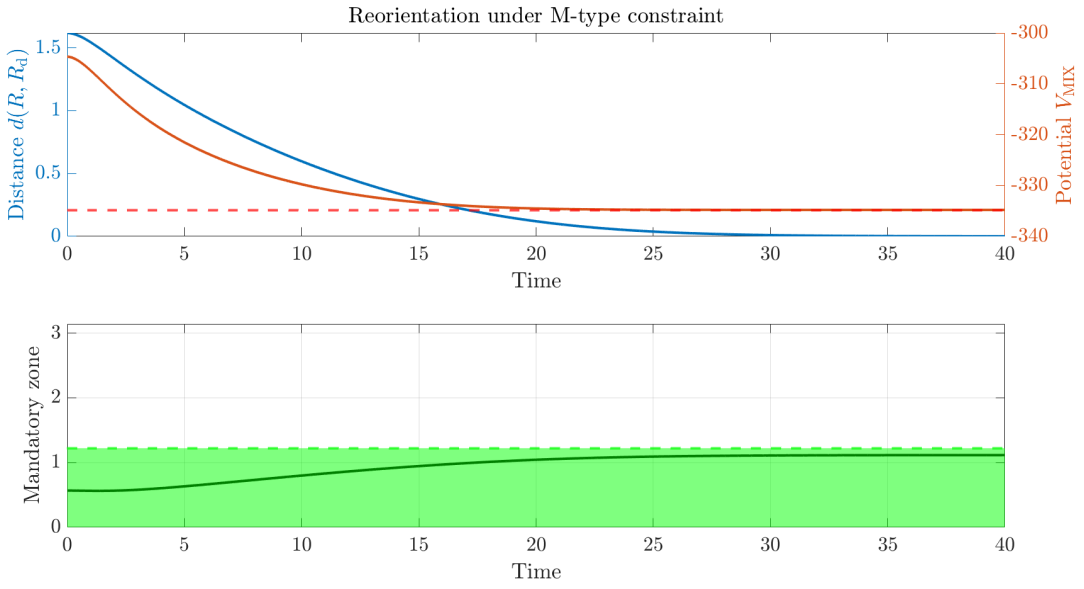

Figure 5.3: Numerical results obtained for the Experiment 1 using mixed additive-multiplicative potential-based control algorithm. Top panel: values of the distance between the actual attitude and the desired attitude, and value of the potential during reorientation; the dashed line represents the theoretically evaluated minimum value of the potential pertaining to this experiment. Bottom panel: Angle between the boresight direction of the antenna and the mandatory direction; the green area represents the mandatory zone. Time is measured in seconds.

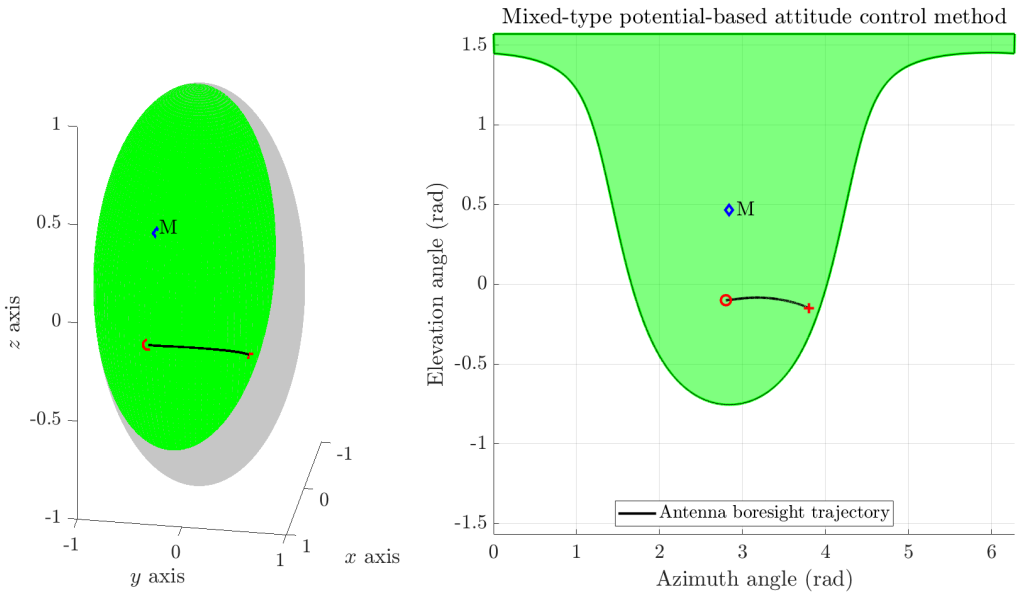

Figure 5.4: Trajectory achieved by the mandatory axis as explained in Experiment 1 using mixed additive-multiplicative potential-based control algorithm. Left panel: The trajectory is shown on a sphere that surrounds the satellite and is centered in the center of gravity of the spacecraft. Right panel: Two-dimensional representation of the sphere, the mandatory zone and the trajectory of the mandatory axis. The red cross represents the attitude reached at the end of the simulation, while the red circle represents the initial attitude.

5.1.2 Experiment 2

The second experiment consisted in simulating reorientation in the presence of four forbidden zones, according to *Case 1a* discussed in the paper [7]. The problem is firstly tackled, again, by an additive-potential-based control algorithm as explained in Section 3.2. In this experiment, the potential and the associated torque read

$$\begin{cases} V_{\mathrm{ADD}}(R) = & -\frac{1}{2}K_{\mathrm{A}}\ell^2 \exp\left(-\frac{d^2(R_{\mathrm{d}},R)}{\ell^2}\right) - K_{\mathrm{F}}\log(\cos\theta_{\mathrm{F1}} - e_{\mathrm{F1}}^{\top}R\,e_{\mathrm{BS}}) \\ & -K_{\mathrm{F}}\log(\cos\theta_{\mathrm{F2}} - e_{\mathrm{F2}}^{\top}R\,e_{\mathrm{BS}}) - K_{\mathrm{F}}\log(\cos\theta_{\mathrm{F3}} - e_{\mathrm{F3}}^{\top}R\,e_{\mathrm{BS}}) \\ & -K_{\mathrm{F}}\log(\cos\theta_{\mathrm{F4}} - e_{\mathrm{F4}}^{\top}R\,e_{\mathrm{BS}}) \\ T_{\mathrm{ADD}}(R) = & -K_{\mathrm{A}}\exp\left(-\frac{d^2(R_{\mathrm{d}},R)}{\ell^2}\right)\mathrm{Log}(R_{\mathrm{d}}^{\top}R) + \frac{K_{\mathrm{F}}}{e_{\mathrm{F1}}^{\top}R\,e_{\mathrm{BS}}-\cos\theta_{\mathrm{F1}}}\sigma(R^{\top}e_{\mathrm{F1}}e_{\mathrm{BS}}^{\top}) \\ & +\frac{K_{\mathrm{F}}}{e_{\mathrm{F2}}^{\top}R\,e_{\mathrm{BS}}-\cos\theta_{\mathrm{F2}}}\sigma(R^{\top}e_{\mathrm{F2}}e_{\mathrm{BS}}^{\top}) + \frac{K_{\mathrm{F}}}{e_{\mathrm{F3}}^{\top}R\,e_{\mathrm{BS}}-\cos\theta_{\mathrm{F3}}}\sigma(R^{\top}e_{\mathrm{F3}}e_{\mathrm{BS}}^{\top}) \\ & +\frac{K_{\mathrm{F}}}{e_{\mathrm{F4}}^{\top}R\,e_{\mathrm{BS}}-\cos\theta_{\mathrm{F4}}}\sigma(R^{\top}e_{\mathrm{F4}}e_{\mathrm{BS}}^{\top}) \end{cases} \tag{5.4}$$

The Table 5.4 shows the data pertaining to this simulation tackled with a virtual additive potential. Notice that, as in the previous experiment, some constants are parameterized to the

inertial coefficient J_{C} for convenience.

Description	Symbol	Numerical value
Initial attitude	R_{i}	$\begin{bmatrix} 0.4726 & -0.3499 & -0.8089 \\ -0.8129 & 0.1814 & -0.5534 \\ 0.3404 & 0.9191 & -0.1987 \end{bmatrix}$
Desired attitude	R_{d}	$\begin{bmatrix} -0.4112 & 0.4083 & 0.8150 \\ 0.8165 & 0.5625 & 0.1302 \\ -0.4053 & 0.7190 & -0.5646 \end{bmatrix}$
Forbidden direction e_{F1}	e_{F1}	$[-0.174\ 0.934\ -0.34]^\top$
Forbidden direction e_{F2}	e_{F2}	$[0\ -0.7071\ 0.7071]^\top$
Forbidden direction e_{F3}	e_{F3}	$[0.8532\ -0.4361\ -0.2861]^\top$
Forbidden direction e_{F4}	e_{F4}	$[-0.1220\ -0.1400\ -0.9830]^\top$
Aperture of the first forbidden cone	θ_{F1}	40 (°)
Aperture of the second forbidden cone	θ_{F2}	40 (°)
Aperture of the third forbidden cone	θ_{F3}	30 (°)
Aperture of the fourth forbidden cone	θ_{F4}	20 (°)
Constant K_{A}	K_{A}	$5 \cdot 10^{-1} J_{\mathrm{C}}$
Constant ℓ^2	ℓ^2	50
Constant K_{f}	K_{f}	$1.5 J_{\mathrm{C}}$
Constant K_{F}	K_{F}	$3.5 \cdot 10^{-2} J_{\mathrm{C}}$

Table 5.4: Numerical data corresponding to the numerical Experiment 2 tackled with a virtual additive potential.

The numerical results obtained with an additive potential are illustrated in the Figure 5.5. The result achieved by the control algorithm in the given time frame is $\mathrm{RPI} = 95.8\%$.

As it may be readily appreciated from the figure, the optimization-based control algorithm effectively attains the minimum value of the potential function while keeping the boresight of the sensor away from the forbidden cones. While the objective of avoiding forbidden areas is accomplished, the desired rotation matrix is not achieved. In fact, from Figure 5.6 can be seen that initially e_{BS} moves towards R_{d} that is signaled by the red cross but when it approaches the directional obstacle the algorithm operates a change of trajectory to avoid entering that area and starts coasting, with a reasonable distance, the forbidden area. Eventually though it struggles to reach the exact orientation as it only swings by the desired attitude. From the top panel of Figure 5.5 it can be seen how the geodetic distance almost reaches zero around 55 seconds in the simulation but then slowly increases and never reaches the goal. Moreover, it can be seen in the bottom left panel how the boresight of the antenna once it gets close to the forbidden area number 3 starts coasting near it while maintaining distance. The combination of the behaviors just explained makes clear that the goal is not reached because two opposites constraints need to be respected. While it is true that through some manual adjustments of the constants a better RPI

can be reached, the problem remains because the trajectory obtained always coasts the forbidden area and then misses the desired attitude.

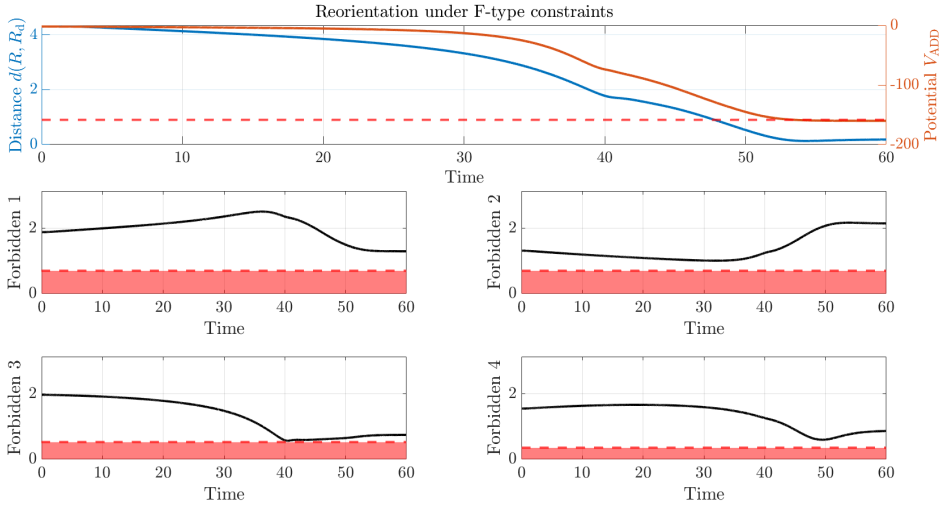

Figure 5.5: Numerical results obtained for the Experiment 2 using an additive-potential-based control algorithm. Top panel: values of the distance between the actual attitude and the desired attitude, and value of the potential during reorientation; the dashed line represents the theoretically evaluated minimum value of the potential pertaining to this experiment. Bottom-left and bottom-right panels: Angle between the boresight direction of the sensor and each forbidden direction; the red areas represent the forbidden zones. Time is measured in seconds.

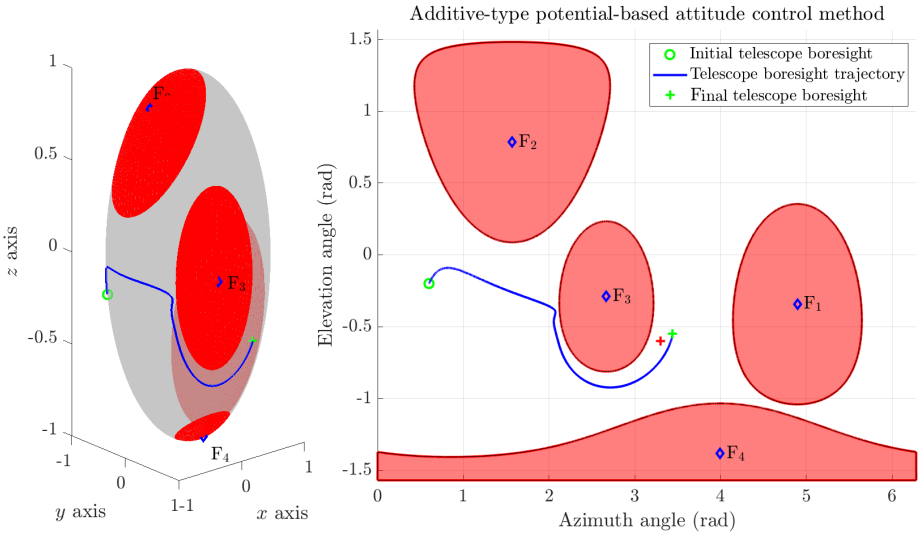

Figure 5.6: Numerical results obtained for the Experiment 2 tackled with a virtual additive potential. Left panel: 3D visualization of boresight trajectory. Right panel: 2D representation of the maneuver. The green cross represents the attitude reached at the end of the simulation, while the green circle represents the initial attitude. The red cross represents the desired attitude.

The same experiment is repeated for mixed-potential explained in Section 3.3 using the same data as additive potential case for initial and desired rotational matrices and also for directional obstacles and amplitudes, instead the torque and the potential read:

$$
\begin{cases}
V_{\mathrm{MIX}}(R) = & -\frac{1}{2}\,K_{\mathrm{A}}\,\ell^2 \exp\left(-\frac{d^2(R\mathrm{d},R)}{\ell^2}\right) - K_{\mathrm{F}}\frac{d^2(R_{\mathrm{d}},R)}{2}(\log(\cos\theta_{\mathrm{F1}} - e_{\mathrm{F1}}^{\top} R\, e_{\mathrm{BS}}) \\
& + \log(\cos\theta_{\mathrm{F2}} - e_{\mathrm{F2}}^{\top} R\, e_{\mathrm{BS}}) + \log(\cos\theta_{\mathrm{F3}} - e_{\mathrm{F3}}^{\top} R\, e_{\mathrm{BS}}) \\
& + \log(\cos\theta_{\mathrm{F4}} - e_{\mathrm{F4}}^{\top} R\, e_{\mathrm{BS}})) \\
T_{\mathrm{MIX}}(R) = & K_{\mathrm{A}} \exp\left(-\frac{d^2(R_{\mathrm{d}},R)}{\ell^2}\right) \mathrm{Log}(R_{\mathrm{d}}^{\top} R) + K_{\mathrm{F}} \log(\cos\theta_{\mathrm{F1}} - e_{\mathrm{F1}}^{\top} R\, e_{\mathrm{BS}}) \\
& + K_{\mathrm{F}} \log(\cos\theta_{\mathrm{F2}} - e_{\mathrm{F2}}^{\top} R\, e_{\mathrm{BS}}) + K_{\mathrm{F}} \log(\cos(\theta_{\mathrm{F3}} - {e_{\mathrm{F3}}}^{\top} R\, e_{\mathrm{BS}}) \\
& + K_{\mathrm{F}} \log(\cos\theta_{\mathrm{F4}} - e_{\mathrm{F4}}^{\top} R\, e_{\mathrm{BS}}) \mathrm{Log}(R_{\mathrm{d}}^{\top} R) \\
& + \frac{d^2(R_{\mathrm{d}},R)}{2}\left(\frac{K_{\mathrm{F}}}{e_{\mathrm{F1}}^{\top} R\, e_{\mathrm{BS}} - \cos\theta_{\mathrm{F1}}}\sigma(R^{\top} e_{\mathrm{F1}} e_{\mathrm{BS}}^{\top}) + \frac{K_{\mathrm{F}}}{e_{\mathrm{F2}}^{\top} R\, e_{\mathrm{BS}} - \cos\theta_{\mathrm{F2}}}\sigma(R^{\top} e_{\mathrm{F2}} e_{\mathrm{BS}}^{\top})\right. \\
& \left. + \frac{K_{\mathrm{F}}}{e_{\mathrm{F3}}^{\top} R\, e_{\mathrm{BS}} - \cos\theta_{\mathrm{F3}}}\sigma(R^{\top} e_{\mathrm{F3}} e_{\mathrm{BS}}^{\top}) + \frac{K_{\mathrm{F}}}{e_{\mathrm{F4}}^{\top} R\, e_{\mathrm{BS}} - \cos\theta_{\mathrm{F4}}}\sigma(R^{\top} e_{\mathrm{F4}} e_{\mathrm{BS}}^{\top})\right)
\end{cases}
\tag{5.5}
$$

while the variables used for this version of the experiment had to be handcrafted and modified to obtain a good-looking trajectory: $K_{\mathrm{A}} = 2 \cdot 10^{-1} J_{\mathrm{C}}$, $\ell^2 = 50$, $K_{\mathrm{f}} = 2 J_{\mathrm{C}}$, $K_{\mathrm{F}} = 2.8 \cdot 10^{-2} J_{\mathrm{C}}$. The result obtained are displayed in Figure 5.8 and also the trajectory obtained is presented in Figure 5.7.

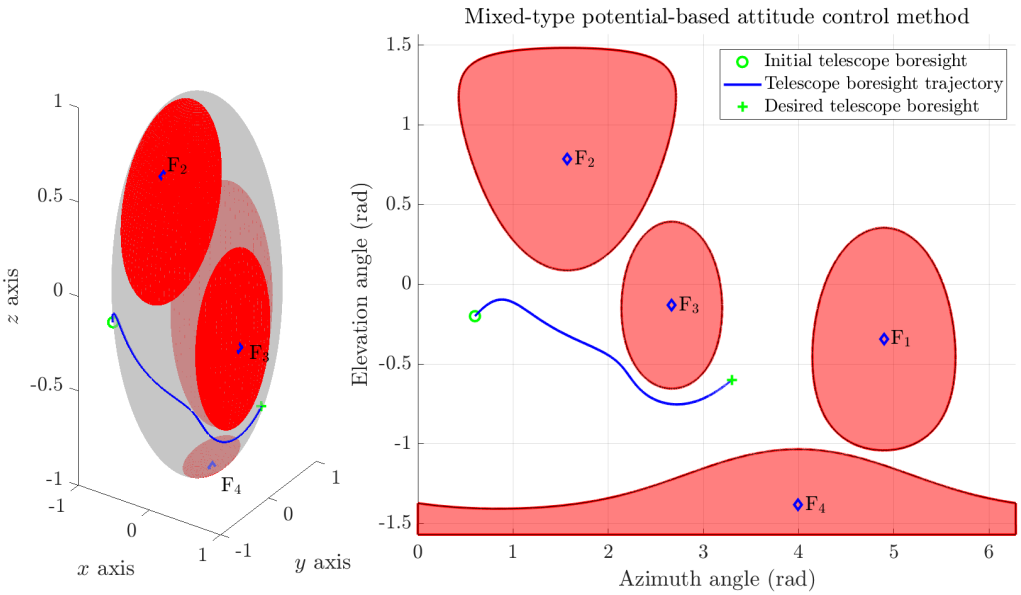

Figure 5.7: Numerical results obtained for the Experiment 2 tackled with a virtual mixed potential. Left panel: 3D visualization of boresight trajectory. Right panel: 2D representation of the maneuver. The green cross represents the attitude reached at the end of the simulation and the desired one, while the green circle represents the initial attitude.

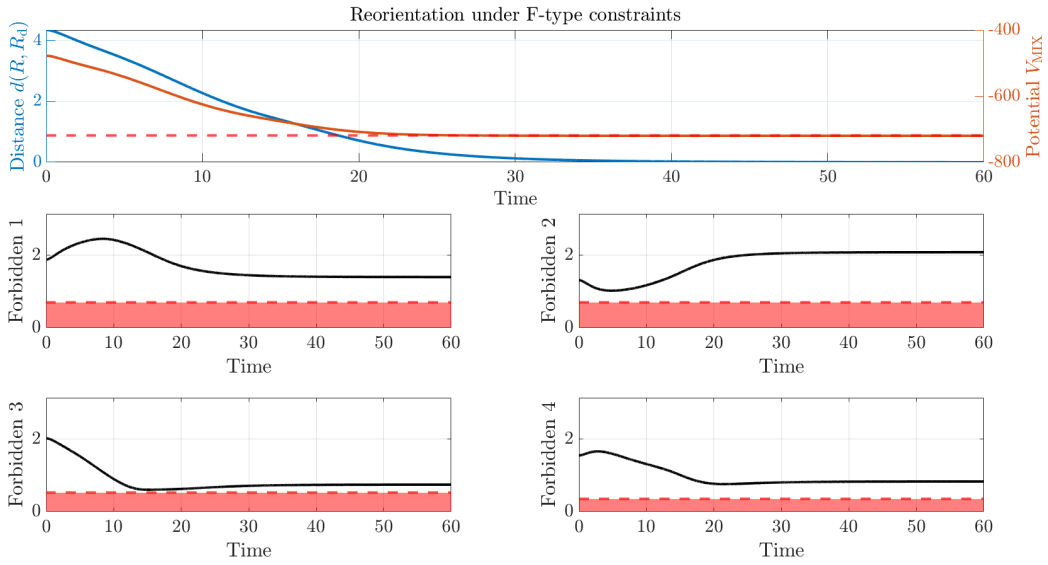

Figure 5.8: Numerical results obtained for the Experiment 2 tackled with a virtual mixed potential. Top panel: values of the distance between the actual attitude and the desired attitude, and value of the potential during reorientation; the dashed line represents the theoretically evaluated minimum value of the potential pertaining to this experiment. Bottom-left and bottom-right panels: Angle between the boresight direction of the sensor and each forbidden direction; the red areas represent the forbidden zones. Time is measured in seconds.

Let be *Trajectory 1* the trajectory accomplished using the additive potential-based control shown in Figure 5.6 and *Trajectory 2* the one accomplished using the mixed potential-based control shown in Figure 5.7. Let now compare the trajectory obtained: firstly, it is important to notice that the desired attitude is reached only using the mixed potential-based control, in fact in Figure 5.7 the red cross marking the desired attitude is not visible since it coincides with the reached attitude signaled with a green cross. Considering the first part of the two trajectories, it is clear that while *Trajectory 1* has a more direct approach to the obstacle (forbidden zone number 3), instead *Trajectory 2* moves towards the obstacle with a direction that has more slope. Comparing the section where the two trajectories coast around the obstacle is visible a similar behavior given that the distance slowly increases towards the end of the simulation. While they have a similar behavior, the result differs because in the coasting phase *Trajectory 1* is longer than *Trajectory 2* resulting in a greater distance from the obstacle and, consequently, from the goal.

5.1.3 Experiment 3

The third experiment concerning reorientation is similar to *Experiment 2* with slight differences in obstacle positions and corresponds to *Case 1b* discussed in the paper [7]. The Table 5.5 displays the values of the constants used in this simulation. In this case the potential and the associated torque are exactly the ones used in *Experiment 2* and are written in equation (5.4).

Description	Symbol	Numerical value
Initial attitude	R_{i}	$\begin{bmatrix} 0.4566 & 0.8892 & 0.0269 \\ 0.3579 & -0.1559 & -0.9207 \\ -0.8145 & 0.4300 & -0.3894 \end{bmatrix}$
Desired attitude	R_{d}	$\begin{bmatrix} -0.8140 & 0.1648 & 0.5570 \\ 0.4620 & -0.3975 & 0.7928 \\ 0.3520 & 0.9027 & 0.2474 \end{bmatrix}$
Forbidden direction e_{F1}	e_{F1}	$[-0.163\ -0.986\ 0.02]^\top$
Forbidden direction e_{F2}	e_{F2}	$[0\ -0.573\ 0.819]^\top$
Forbidden direction e_{F3}	e_{F3}	$[0.067\ 0.462\ -0.88]^\top$
Forbidden direction e_{F4}	e_{F4}	$[0.813\ -0.548\ -0.19]^\top$
Aperture of the first forbidden cone	θ_{F1}	40 (°)
Aperture of the second forbidden cone	θ_{F2}	40 (°)
Aperture of the third forbidden cone	θ_{F3}	20 (°)
Aperture of the fourth forbidden cone	θ_{F4}	20 (°)
Initial angular speed		0_3

Table 5.5: Numerical data corresponding to the numerical Experiment 3.

As a first attempt, the problem is tackled by an additive-potential-based control algorithm as explained in Section 3.2. The values of the coefficients chosen in this experiment are $K_{\mathrm{A}} = 4.5 \cdot 10^{-1} J_{\mathrm{C}}$, $\ell^2 = 50$, $K_{\mathrm{f}} = 3J_{\mathrm{C}}$, $K_{\mathrm{F}} = 0.1 \cdot 10^{-3} J_{\mathrm{C}}$.

The numerical results obtained with an additive potential are illustrated in the Figure 5.9 and the trajectory achieved is shown in Figure 5.10. The optimization-based control algorithm effectively attains the minimum value of the potential function while keeping the boresight of the sensor away from the forbidden cones, moreover the result achieved by the control algorithm in the given time frame is $\mathrm{RPI} = 100\%$.

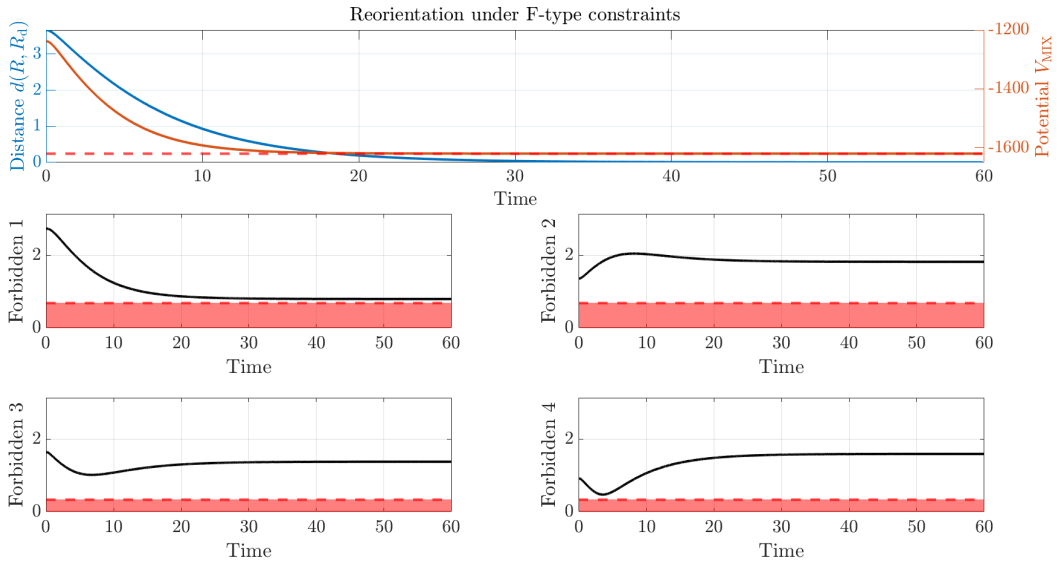

Figure 5.9: Numerical results obtained for the Experiment 3 tackled with a virtual additive potential. Top-left panel: values of the distance between the actual attitude and the desired attitude, and value of the potential during reorientation; the dashed line represents the theoretically evaluated minimum value of the potential pertaining to this experiment. Bottom-left and bottom-right panels: Angle between the boresight direction of the sensor and each forbidden direction; the red areas represent the forbidden zones. Time is measured in seconds.

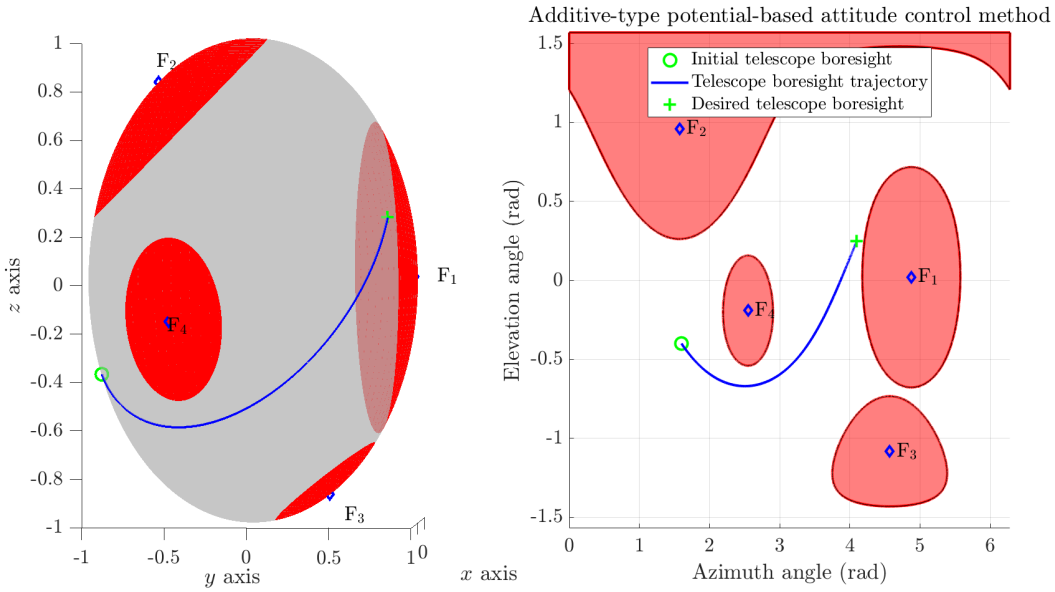

Figure 5.10: Numerical results obtained for the Experiment 3 tackled with a virtual additive potential. Left panel: 3D visualization of boresight trajectory. Right panel: 2D representation of the maneuver. The green cross represents the attitude reached at the end of the simulation and the desired one, while the green circle represents the initial attitude.

As a further attempt, the problem is tackled by a mixed additive-multiplicative potential-based approach, as explained in Section 3.3. In this experiment, the potential and the associated torque read

$$
\begin{cases}
V_{\mathrm{MIX}}(R) = & -\frac{1}{2}\,K_{\mathrm{A}}\,\ell^2 \exp\left(-\frac{d^2(R\mathrm{d},R)}{\ell^2}\right) - K_{\mathrm{F}}\frac{d^2(R_{\mathrm{d}},R)}{2}(\log(\cos\theta_{\mathrm{F1}} - e_{\mathrm{F1}}^{\top} R\, e_{\mathrm{BS}}) \\
& + \log(\cos\theta_{\mathrm{F2}} - e_{\mathrm{F2}}^{\top} R\, e_{\mathrm{BS}}) + \log(\cos\theta_{\mathrm{F3}} - e_{\mathrm{F3}}^{\top} R\, e_{\mathrm{BS}}) \\
& + \log(\cos\theta_{\mathrm{F4}} - e_{\mathrm{F4}}^{\top} R\, e_{\mathrm{BS}})) \\
T_{\mathrm{MIX}}(R) = & -K_{\mathrm{A}} \exp\left(-\frac{d^2(R_{\mathrm{d}},R)}{\ell^2}\right) \mathrm{Log}(R_{\mathrm{d}}^{\top} R) + K_{\mathrm{F}} \log(\cos\theta_{\mathrm{F1}} - e_{\mathrm{F1}}^{\top} R\, e_{\mathrm{BS}}) \\
& + K_{\mathrm{F}} \log(\cos\theta_{\mathrm{F2}} - e_{\mathrm{F2}}^{\top} R\, e_{\mathrm{BS}}) + K_{\mathrm{F}} \log(\cos(\theta_{\mathrm{F3}} - {e_{\mathrm{F3}}}^{\top} R\, e_{\mathrm{BS}}) \\
& + K_{\mathrm{F}} \log(\cos\theta_{\mathrm{F4}} - e_{\mathrm{F4}}^{\top} R\, e_{\mathrm{BS}}) \mathrm{Log}(R_{\mathrm{d}}^{\top} R) \\
& + \frac{d^2(R_{\mathrm{d}},R)}{2}\left(\frac{K_{\mathrm{F}}}{e_{\mathrm{F1}}^{\top} R\, e_{\mathrm{BS}} - \cos\theta_{\mathrm{F1}}}\sigma(R^{\top} e_{\mathrm{F1}} e_{\mathrm{BS}}^{\top}) + \frac{K_{\mathrm{F}}}{e_{\mathrm{F2}}^{\top} R\, e_{\mathrm{BS}} - \cos\theta_{\mathrm{F2}}}\sigma(R^{\top} e_{\mathrm{F2}} e_{\mathrm{BS}}^{\top})\right) \\
& + \frac{K_{\mathrm{F}}}{e_{\mathrm{F3}}^{\top} R\, e_{\mathrm{BS}} - \cos\theta_{\mathrm{F3}}}\sigma(R^{\top} e_{\mathrm{F3}} e_{\mathrm{BS}}^{\top}) + \frac{K_{\mathrm{F}}}{e_{\mathrm{F4}}^{\top} R\, e_{\mathrm{BS}} - \cos\theta_{\mathrm{F4}}}\sigma(R^{\top} e_{\mathrm{F4}} e_{\mathrm{BS}}^{\top}))
\end{cases}
\tag{5.6}
$$

The values of the coefficients chosen in this experiment are $K_{\mathrm{A}} = 2.7 \cdot 10^{-1} J_{\mathrm{C}}$ $K_{\mathrm{f}} = 2J_{\mathrm{C}}$, $K_{\mathrm{F}} = 1 \cdot 10^{-3} J_{\mathrm{C}}$.

The numerical results obtained are illustrated in the Figure 5.12 while the trajectory completed is represented in Figure 5.11.

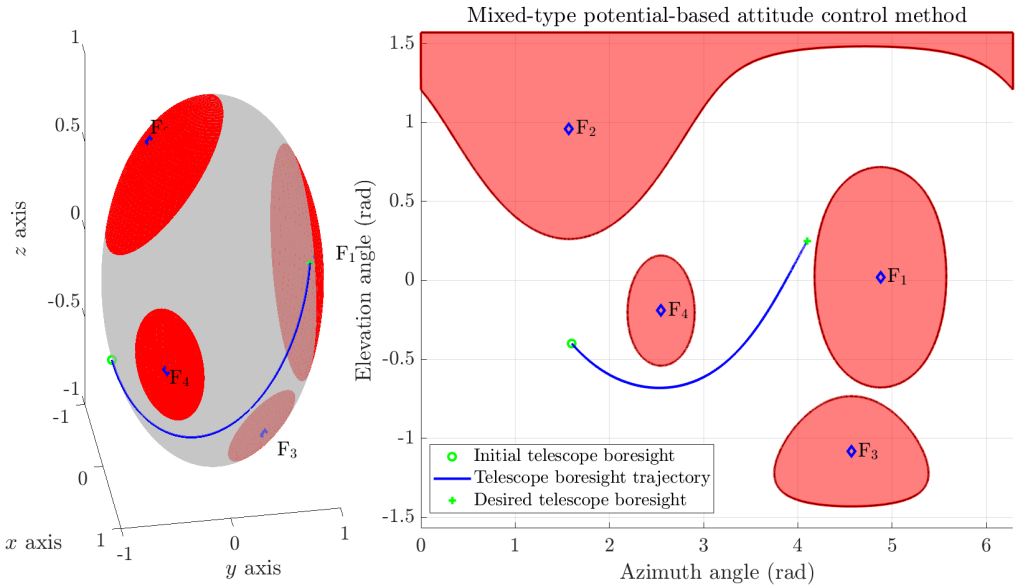

Figure 5.11: Numerical results obtained for the Experiment 3 tackled with a virtual mixed additive-multiplicative potential. Left panel: 3D visualization of boresight trajectory. Right panel: 2D representation of the maneuver. The green cross represents the attitude reached at the end of the simulation and the desired one, while the green circle represents the initial attitude.

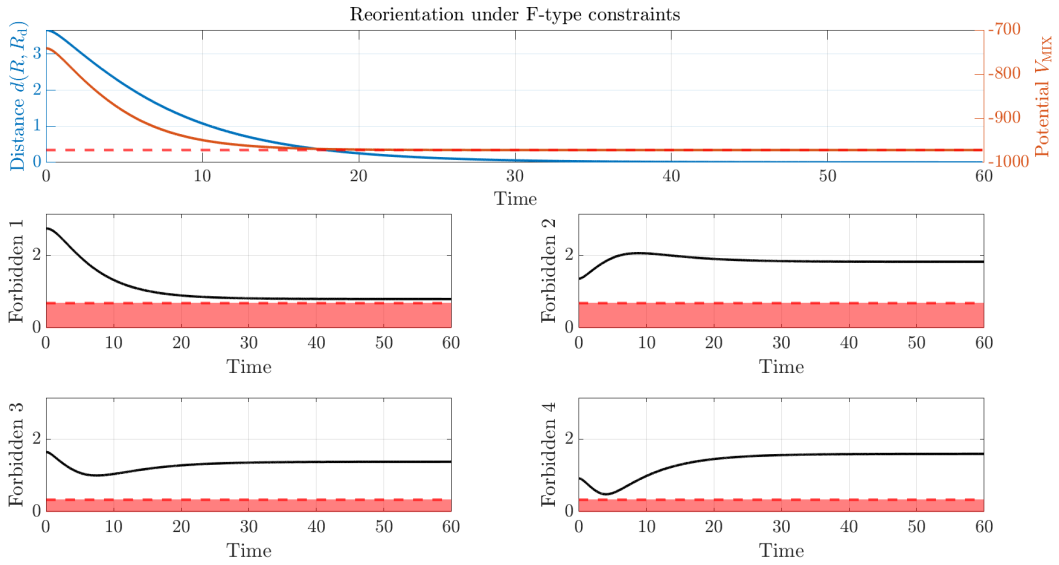

Figure 5.12: Numerical results obtained for the Experiment 3 tackled with a virtual mixed additive-multiplicative potential. Top-left panel: values of the distance between the actual attitude and the desired attitude, and value of the potential during reorientation. Bottom-left and right-hand panels: Angle between the boresight direction of the sensor and each forbidden direction; the red areas represent forbidden zones. Time is measured in seconds.

In this experiment, the result achieved by the control algorithm in the given time frame is $\mathrm{RPI} = 100\%$. In this case using two different potential-based controls does not show any particular convenience supplying almost the exact trajectories and data.

5.1.4 Experiment 4

The fourth experiment concerning reorientation is based on a mandatory zone and three forbidden zones, it corresponds to *Case 3* discussed in the paper [7]. The Table 5.6 shows the reorientation data pertaining to this simulation, firstly completed using an additive potential-based control algorithm using the following equations:

$$\begin{cases} V_{\mathrm{ADD}}(R) = & -\frac{1}{2}K_{\mathrm{A}}\ell^2 \exp\left(-\frac{d^2(R_{\mathrm{d}},R)}{\ell^2}\right) - K_{\mathrm{F}}\log(\cos\theta_{\mathrm{F1}} - e_{\mathrm{F1}}^{\top}R\,e_{\mathrm{BS}}) \\ & -K_{\mathrm{F}}\log(\cos\theta_{\mathrm{F2}} - e_{\mathrm{F2}}^{\top}R\,e_{\mathrm{BS}}) - K_{\mathrm{F}}\log(\cos\theta_{\mathrm{F3}} - e_{\mathrm{F3}}^{\top}R\,e_{\mathrm{BS}}) \\ & -K_{\mathrm{M}}\log(e_{\mathrm{M}}^{\top}R\,e_{\mathrm{BA}} - \cos\theta_{\mathrm{M}}) \\ T_{\mathrm{ADD}}(R) = & -K_{\mathrm{A}}\exp\left(-\frac{d^2(R_{\mathrm{d}},R)}{\ell^2}\right)\mathrm{Log}(R_{\mathrm{d}}^{\top}R) + \frac{K_{\mathrm{F}}}{e_{\mathrm{F1}}^{\top}R\,e_{\mathrm{BS}}-\cos\theta_{\mathrm{F1}}}\sigma(R^{\top}e_{\mathrm{F1}}e_{\mathrm{BS}}^{\top}) \\ & +\frac{K_{\mathrm{F}}}{e_{\mathrm{F2}}^{\top}R\,e_{\mathrm{BS}}-\cos\theta_{\mathrm{F2}}}\sigma(R^{\top}e_{\mathrm{F2}}e_{\mathrm{BS}}^{\top}) + \frac{K_{\mathrm{F}}}{e_{\mathrm{F3}}^{\top}R\,e_{\mathrm{BS}}-\cos\theta_{\mathrm{F3}}}\sigma(R^{\top}e_{\mathrm{F3}}e_{\mathrm{BS}}^{\top}) \\ & +\frac{K_{\mathrm{M}}}{e_{\mathrm{M}}^{\top}R\,e_{\mathrm{BA}}-\cos\theta_{\mathrm{M}}}\sigma(R^{\top}e_{\mathrm{M}}e_{\mathrm{BA}}^{\top}) \end{cases} \tag{5.7}$$

Description	Numerical value
Initial attitude R_{i}	$(0.714, 0.637, 0.13, -0.26)$
Desired attitude R_{d}	$(-0.23, -0.08, -0.491, 0.84)$
Mandatory direction e_{M}	$[0.813 \ -0.548 \ -0.192]^{\top}$
Forbidden direction e_{F1}	$[0\ 1\ 0]^{\top}$
Forbidden direction e_{F2}	$[0 \ -0.819\ 0.573]^{\top}$
Forbidden direction e_{F3}	$[0.122\ 0.139 \ -0.982]^{\top}$
Aperture of the mandatory cone θ_{M}	70 (°)
Aperture of the first forbidden cone θ_{F1}	40 (°)
Aperture of the second forbidden cone θ_{F2}	40 (°)
Aperture of the third forbidden cone θ_{F3}	20 (°)
Initial angular speed	0_3

Table 5.6: Numerical data corresponding to the numerical Experiment 4 using an additive potential-based control algorithm. The rotation matrices are expressed in JPL quaternion notation for the sake of notation conciseness.

The values of the coefficients chosen in this experiment are $K_{\mathrm{A}} = 4.5 \cdot 10^{-2} J_{\mathrm{C}}$, $\ell^2 = 50$, $K_{\mathrm{f}} = 1.8 J_{\mathrm{C}}$, $K_{\mathrm{M}} = 4 \cdot 10^{-3} J_{\mathrm{C}}$, $K_{\mathrm{F}} = 6 \cdot 10^{-3} J_{\mathrm{C}}$. The results obtained with an additive potential are illustrated in the Figure 5.14 while in Figure 5.13 is displayed the trajectory of the evolution of the attitude projected in two dimensions.

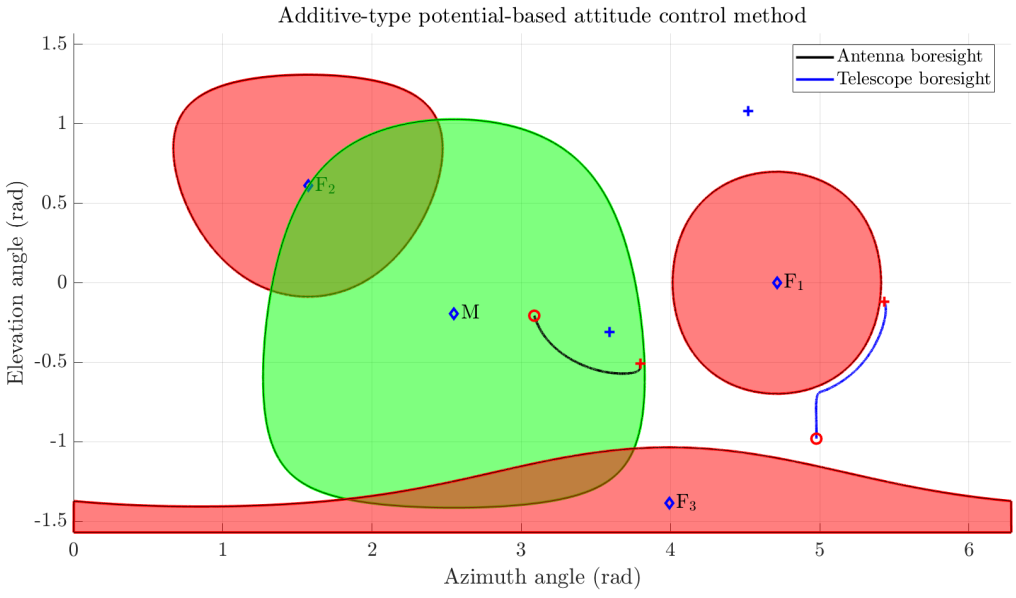

Figure 5.13: Trajectory obtained for Experiment 4 tackled with a virtual additive potential. The two red circles at the start of antenna and telescope trajectories represent their start points, while the red crosses represent the final points of the two. The blue crosses are the desired final points for the boresight of the already mentioned instrumentation.

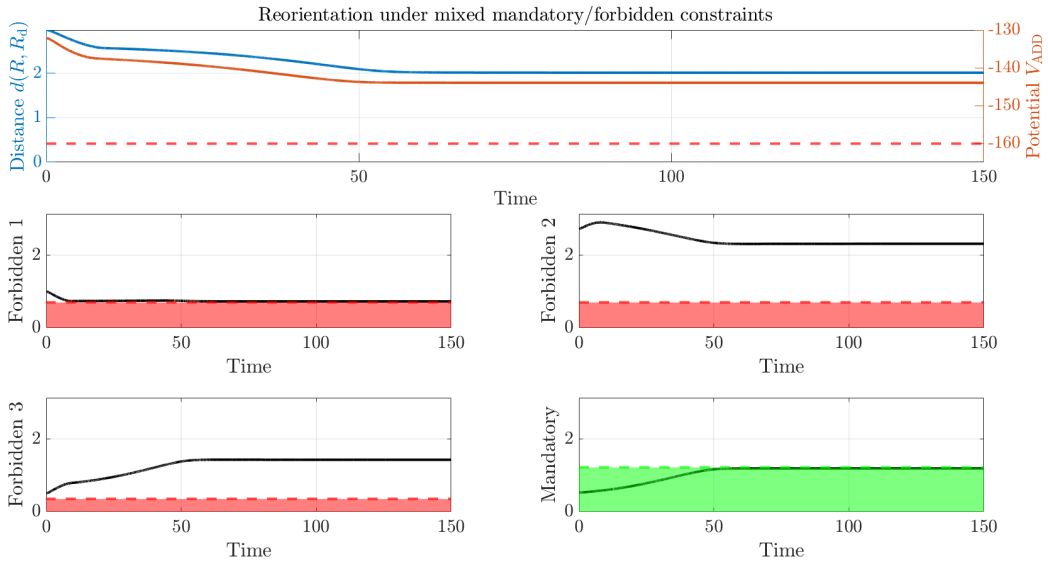

Figure 5.14: Numerical results obtained for the Experiment 4 tackled with a virtual additive potential. Top-left panel: values of the distance between the actual attitude and the desired attitude, and value of the potential during reorientation; the dashed line represents the theoretically evaluated minimum value of the potential pertaining to this experiment. Bottom-left and bottom-right panels: Angle between the boresight direction of the sensor and each forbidden direction, as well as angle between the boresight direction of the antenna and the mandatory direction; the red areas represent the forbidden zones, while the green area represent the mandatory zone. Time is measured in seconds.

While the optimization-based control algorithm effectively keeps the boresight of the sensor away from the forbidden cones and the boresight of the antenna within the mandatory zone, the attained orientation does not match at all the desired one and also the algorithm is not able to reach the minimum of the potential function. In fact, the result achieved by the control algorithm in the given time frame is only $\mathrm{RPI} = 32.3\%$.

As a further attempt, the problem is tackled by a mixed additive-multiplicative potential-based approach, as explained in Section 3.3. The values of the coefficients chosen in this experiment are $K_{\mathrm{f}} = 2.5 J_{\mathrm{C}}$, $K_{\mathrm{M}} = 1.5 \cdot 10^{-1} J_{\mathrm{C}}$, $K_{\mathrm{F}} = 1.2 \cdot 10^{-2} J_{\mathrm{C}}$. The numerical results obtained are illustrated in the Figure 5.15 and the trajectory is displayed in Figure 5.16 while

the potential and torque related to this experiment read:

$$
\begin{cases}
V_{\mathrm{MIX}}(R) = & -\frac{1}{2}\,K_{\mathrm{A}}\,\ell^2\exp\left(-\frac{d^2(R\mathrm{d},R)}{\ell^2}\right) - \frac{1}{2}\,d^2(R\mathrm{d},R)\,(K_{\mathrm{M}}\log(e_{\mathrm{M}}^{\top}R\,e_{\mathrm{BA}} - \cos\theta_{\mathrm{M}}) \\
& + K_{\mathrm{F}}\log(\cos\theta_{\mathrm{F1}} - e_{\mathrm{F1}}^{\top}R\,e_{\mathrm{BS}}) + K_{\mathrm{F}}\log(\cos\theta_{\mathrm{F2}} - e_{\mathrm{F2}}^{\top}R\,e_{\mathrm{BS}}) \\
& + K_{\mathrm{F}}\log(\cos\theta_{\mathrm{F3}} - e_{\mathrm{F3}}^{\top}R\,e_{\mathrm{BS}}) + K_{\mathrm{F}}\log(\cos\theta_{\mathrm{F4}} - e_{\mathrm{F4}}^{\top}R\,e_{\mathrm{BS}})) \\
T_{\mathrm{MIX}}(R) = & -K_{\mathrm{A}}\exp\left(-\frac{d^2(R_{\mathrm{d}},R)}{\ell^2}\right)\mathrm{Log}(R_{\mathrm{d}}^{\top}R) + K_{\mathrm{F}}\log(\cos\theta_{\mathrm{F1}} - e_{\mathrm{F1}}^{\top}R\,e_{\mathrm{BS}}) \\
& + K_{\mathrm{F}}\log(\cos\theta_{\mathrm{F2}} - e_{\mathrm{F2}}^{\top}\,R\,e_{\mathrm{BS}}) + K_{\mathrm{F}}\log(\cos\theta_{\mathrm{F3}} - {e_{\mathrm{F3}}}^{\top}\,R\,e_{\mathrm{BS}}) \\
& + K_{\mathrm{F}}\log(\cos\theta_{\mathrm{F4}} - e_{\mathrm{F4}}^{\top}\,R\,e_{\mathrm{BS}})\mathrm{Log}(R_{\mathrm{d}}^{\top}\,R) \\
& + \frac{d^2(R_{\mathrm{d}},R)}{2}\Big(\frac{K_{\mathrm{F}}}{e_{\mathrm{F1}}^{\top}R\,e_{\mathrm{BS}}-\cos\theta_{\mathrm{F1}}}\sigma(R^{\top}e_{\mathrm{F1}}e_{\mathrm{BS}}^{\top}) + \frac{K_{\mathrm{F}}}{e_{\mathrm{F2}}^{\top}R\,e_{\mathrm{BS}}-\cos\theta_{\mathrm{F2}}}\sigma(R^{\top}e_{\mathrm{F2}}e_{\mathrm{BS}}^{\top}) \\
& + \frac{K_{\mathrm{F}}}{e_{\mathrm{F3}}^{\top}R\,e_{\mathrm{BS}}-\cos\theta_{\mathrm{F3}}}\sigma(R^{\top}e_{\mathrm{F3}}e_{\mathrm{BS}}^{\top}) + \frac{K_{\mathrm{F}}}{e_{\mathrm{F4}}^{\top}R\,e_{\mathrm{BS}}-\cos\theta_{\mathrm{F4}}}\sigma(R^{\top}e_{\mathrm{F4}}e_{\mathrm{BS}}^{\top})).
\end{cases}
\tag{5.8}
$$

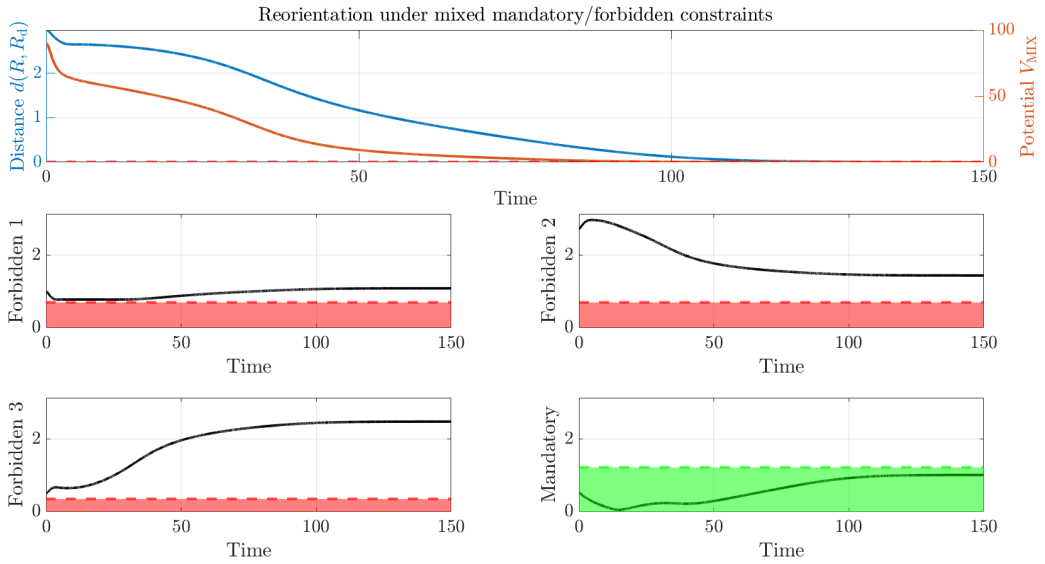

Figure 5.15: Numerical results obtained for the Experiment 4 tackled with a virtual mixed additive-multiplicative potential. Top-left panel: values of the distance between the actual attitude and the desired attitude, and value of the potential during reorientation. Bottom-left and bottom-right panels: Angle between the boresight direction of the sensor and each forbidden direction, as well as angle between the boresight direction of the antenna and the mandatory direction; the red areas represent forbidden zones, while the green area represent the mandatory zone. Time is measured in seconds.

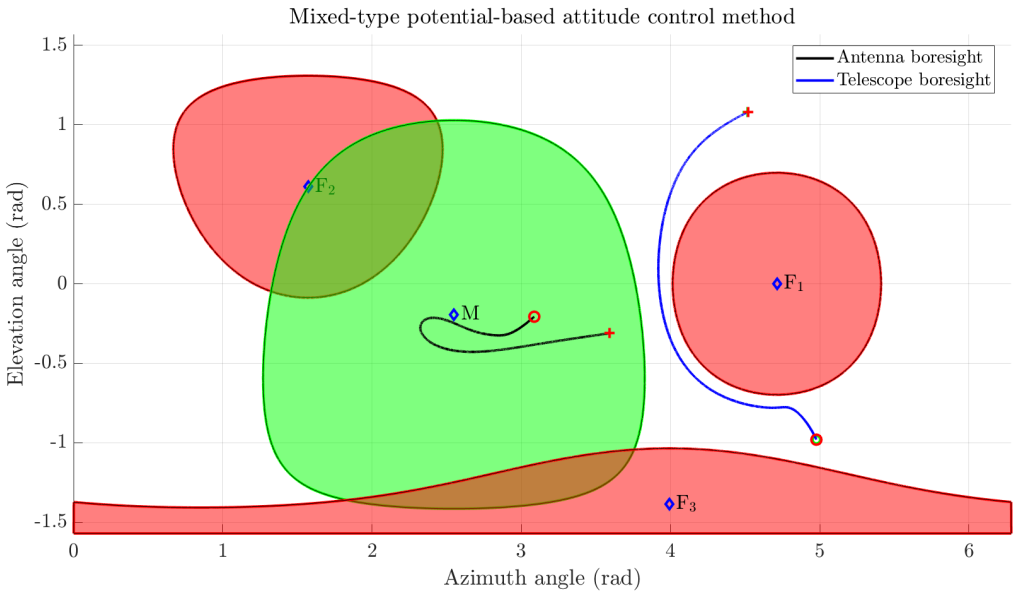

Figure 5.16: Trajectory obtained for the Experiment 4 tackled with a virtual mixed additive-multiplicative potential. The two red circles at the start of antenna and telescope trajectories represent their start points, while the red crosses represent the final and desired points of the two.

The result achieved by the control algorithm in the given time frame is $\mathrm{RPI} = 100\%$.

The difference between the two strategies is substantial, in fact, the trajectories follow two completely different paths and end up with very different RPI percentages. In the additive potential case, the path chosen by the algorithm makes the boresight of the telescope go towards the right of the first forbidden zone as seen in Figure 5.13 while instead in the mixed potential case the telescope boresight goes towards the left of the obstacle. By going to the right of the obstacle, in Figure 5.13, is clear that the trajectory in the given time frame stops (before reaching the desired attitude signaled with blue crosses) in such way that the telescope boresight is very close to the first forbidden zone while the antenna boresight is very close to the barrier of the mandatory zone, this is due to physical constraints. In fact, the trajectory encounters a point in which the satellite physically cannot go beyond because the angle between the right most outer parts of the forbidden zone and the mandatory zone is greater than the angle between the boresight of the antenna and the telescope and if the algorithm decides to iterate over the points marked with the two red crosses (one in the mandatory zone and one near the first forbidden zone), one constraint of the two would be broken and either the antenna would exit the mandatory zone or the telescope would fall inside the obstacle. To better understand the situation, we can use Figure 5.14 as reference where is noticeable in the bottom panels two particular behaviors of the mandatory and forbidden angles that just skim the surface of respectively, the green and red areas, denoting that the constraints are really close to be broken. In the case tackled with a

virtual mixed potential, instead, the algorithm runs a different approach. It makes the telescope boresight pass through the left side of the first obstacle, in this manner the antenna boresight is free to move at first away from the desired attitude and once the telescope has avoided the obstacle, both boresight can finally move towards the desired attitude while satisfying both constraints given (this time the two red crosses overlap the two blue crosses in Figure 5.13 because the attitude reached coincides with the desired one).

5.2 Numerical simulations about rendezvous

A number of experiments concerning rendezvous are performed. A first set of experiments are performed in the presence of obstacles whose position is fixed with respect to the reference frame $\mathcal{F}_{\mathrm{S}}$. A second set of experiments are devoted to testing the behavior of the guidance algorithm in the presence of moving obstacles. A third set of experiments are, instead, dedicated to evaluating the performance of a guidance strategy that consists in joint translation and attitude control.

5.2.1 Experiment 1

The first experiment is performed by assuming the presence of obstacles whose position is fixed with respect to the reference frame $\mathcal{F}_{\mathrm{S}}$. The aim of this experiment is to compare the performances of the three control strategies described in Section 4.1 in terms of propellant consumption. In this experiment, it is set $h = 0.01$ (sec).

The initial location, desired location and initial speed are summarized in Table 5.7.

Description	Symbol	Value
Initial location	p_{i}	$[-16{,}100\ 0\ 3{,}000]^{\top}$ (m)
Initial speed	$\dot{p}_{\mathrm{i}}$	$[-0.5\ 0\ 0.01]^{\top}$ (m/s)
Desired location	p_{d}	$[0\ 0\ 150]^{\top}$ (m)

Table 5.7: Reference values for the Experiment 1 about cruising phase. Recalling that the Z (or R_{bar}) axis points toward the Earth, hence a quota of 150 m in the LVLH reference frame indicates a target location below the station (as seen from the Earth).

Notice that the control algorithm is implemented in such a way that the cruising phase is deemed concluded whenever the distance between the spacecraft and the target is less than 50 m.

The Table 5.8 shows the location of four obstacles along with their safety radius.

Safety radius (m)	Location (m)
$\eta_1 = 650$ (m)	$o_1 = [-10,000\ 0\ 1,500]^\top$ (m)
$\eta_2 = 350$ (m)	$o_2 = [-5,500\ 0\ 1900]^\top$ (m)
$\eta_3 = 150$ (m)	$o_3 = [-2,800\ 0\ 0]^\top$ (m)
$\eta_4 = 50$ (m)	$o_4 = [-2,100\ 0\ 200]^\top$ (m)

Table 5.8: Location and safety radius of the obstacles ordered by size. All obstacles happen to locate below the station (as seen from the Earth).

In this experiment, the components of the random disturbance F_{rd} are zero-mean random Gaussian variables with standard deviation of 100 N. Notice that the random disturbance takes a non-zero component along the y axis, henceforth the motion of the spacecraft will take place slightly off the $x-z$ plane and the control algorithm will need to compensate for such unwanted effect (the desired position is located on the vertical plane, in fact).

The numerical results are illustrated in Figure 5.17, which shows the trajectory of the spacecraft along the $x-z$ plane in the LVLH coordinate frame, and in Figure 5.18, which shows the trajectory of the spacecraft along the landscape of the virtual potential function used to achieve automated guidance.

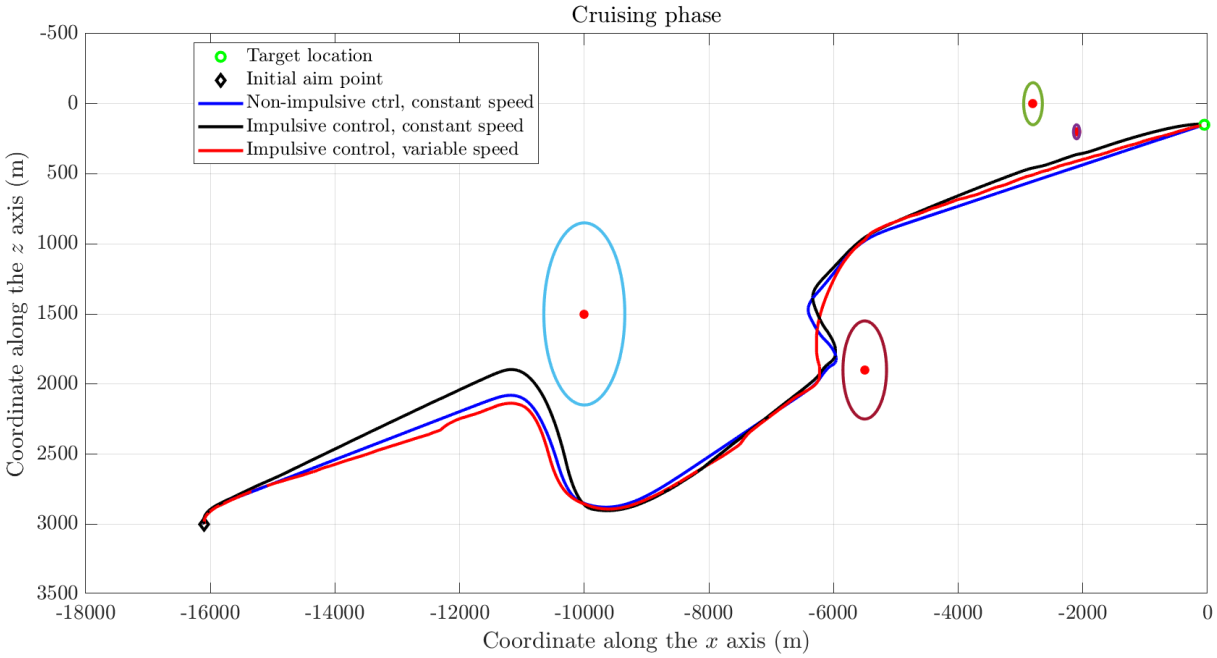

Figure 5.17: Numerical results obtained for the Experiment 1 about cruising phase: Trajectory in the LVLH coordinate frame. Reminding that the X (or V_{bar}) axis points toward the direction of motion over the orbit, hence a negative value of the x coordinate indicates a spacecraft that is, in fact, chasing the space station from behind. The ovals denote the boundaries of the safety regions surrounding each obstacle.

In particular, the Figure 5.17 shows how the spacecraft is enabled to traverse the space, keeping sufficiently far from the obstacles while approaching the target location. The results displayed in this figure show that, in the absence of obstacles, the spacecraft is driven to take the shortest router, except that, in the vicinity of the obstacles, the spacecraft is forced to turn around the safety surface of the obstacles found on its path, hence taking a detour from a straight path. The degree of curvature depends certainly on the chosen values of the parameters, which may be subject to a more or less conservative design, and on the safety radii of the obstacle which, to some extent, depend on the sensitivity range of the sensors mounted aboard the spacecraft. Notice that it is assumed that the space station has mapping abilities and provides a detailed map of the main obstacles sites and sizes so that a spacecraft endowed with proximity sensors may safely navigate through them.

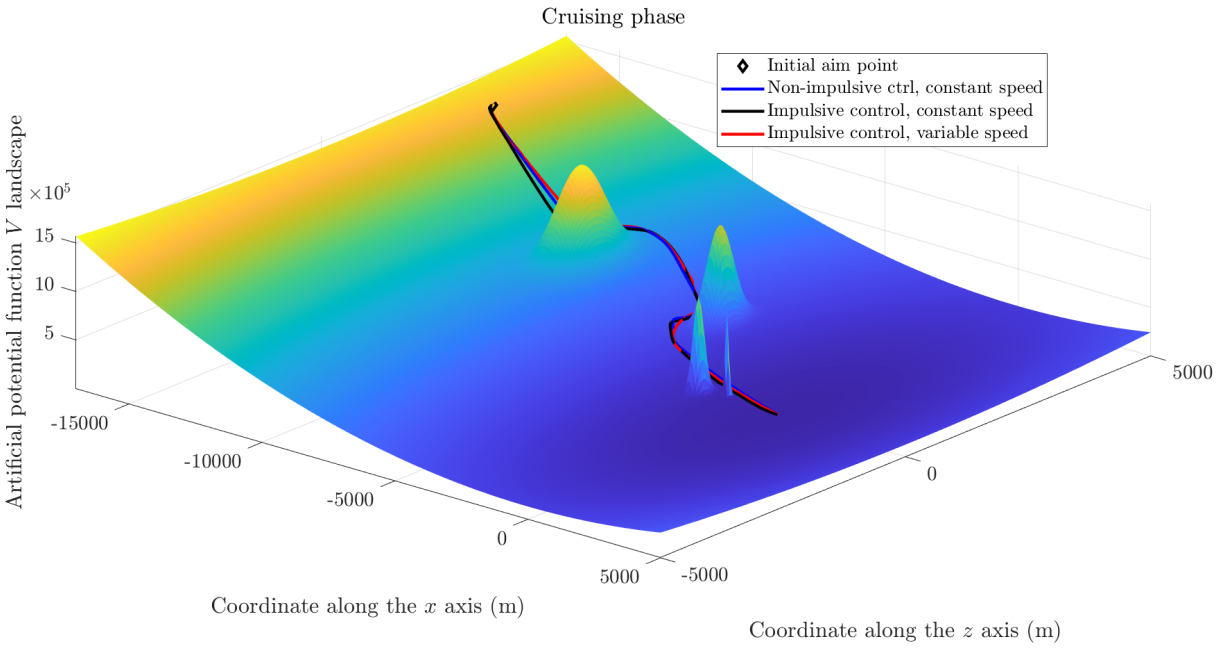

Figure 5.18: Numerical results obtained for the Experiment 1 about cruising phase: Trajectory along the landscape of the virtual potential function.

On the other hand, the Figure 5.18 serves to illustrate the shape and the function of the devised potential energy function. The landscape of the potential presents a global minimum corresponding to the desired location, as well as four peaks in correspondence to the obstacles' central location. The trajectory of the spacecraft develops bypassing the areas of higher potential while "rolling down" toward the minimal-potential location.

Such results are obtained by setting the values of the parameters defined in the context of attractive-repulsive potential as $H_{\mathrm{A}} = 10^{-2}$ and $H_{\mathrm{R}} = 10^{6}$. Obtained trajectories appear quite similar to one another and the three control strategies are able to achieve the desired location

where the cruising phase ends.

However, the consumption of propellant resulting from the application of the three control strategies results to be quite different. The consumption resulting from the three regulation strategies are displayed in the Figure 5.19. The introduction of impulsive control hence results in a sensible reduction of propellant consumption compared to non-impulsive regulation. Furthermore, the reduction of total mass corresponding to the regulation algorithm based on impulsive control and variable desired speed compared to the constant-speed case is similar and depending on different cases it produces a better or worse performance. This happens because of a different behavior at the end of cruising phase, while the first control, thanks to its lowest speed at the end of cruising phase, follows the desired direction and so takes a shorter route to the far-end phase end point, the second control is less affected by any changes of trajectory due to a higher speed and follows a wider path to reach the desired point.

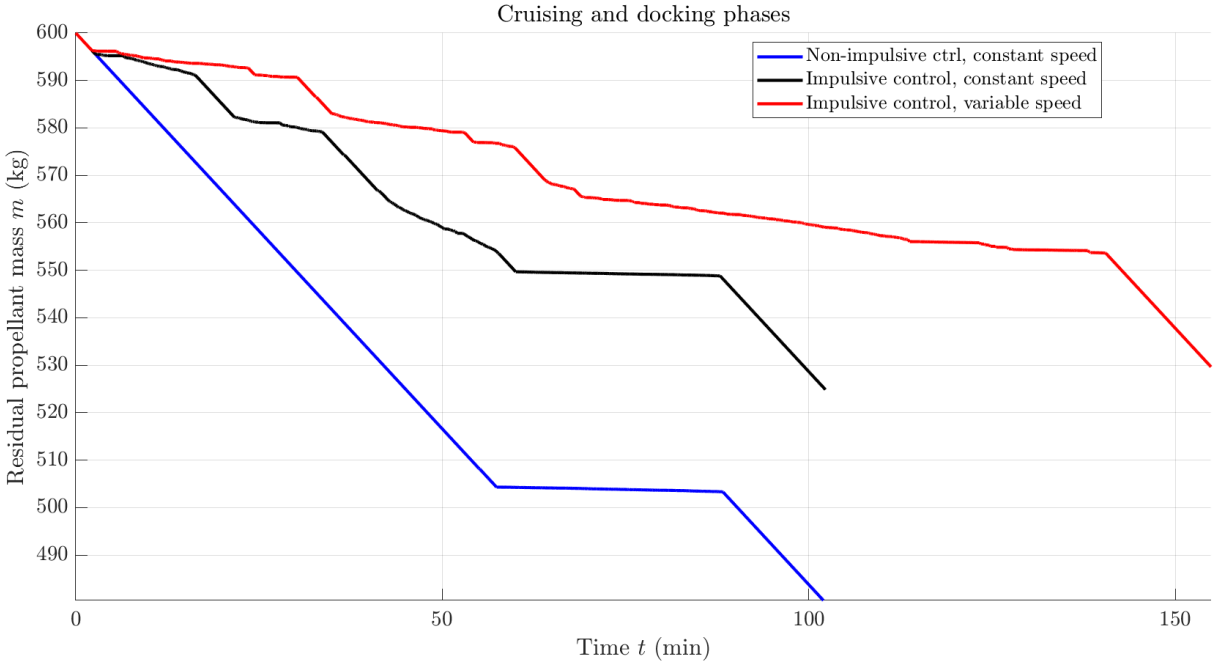

Figure 5.19: Numerical results obtained for the Experiment 1 about cruising phase: Cold gas consumption.

A further element of evaluation of the control strategies under comparison is the final speed upon reaching the predefined target location. No control requirements are defined on this matter, hence the control strategies do not embody any information about a final desired speed. However, the regulation strategy based on variable speed implicitly makes the final speed vanish to zero since it is proportional to the distance to the target. The effects of explicit speed limitation are illustrated in the Figure 5.20, from which it is apparent how, in this instance, the spacecraft arrives ready to start the docking sequence.

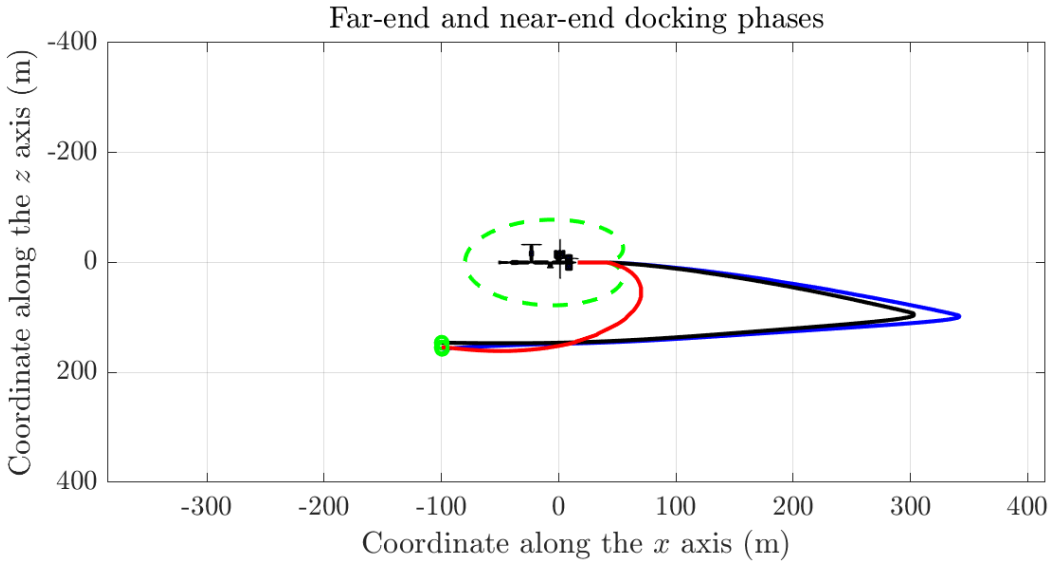

Figure 5.20: Numerical results obtained for the Experiment 1 about cruising phase: Detail of the final guidance maneuver to attain docking. The color code is the same as in previous figures concerning Experiment 1. $H_{\mathrm{t}} = 1$ for all the docking phase.

The position at which the far-end maneuver stops is indicated as $p_{\mathrm{fe}} \in \mathbb{R}^3 = [40\ 0\ 0]^\top$ (m), while the position at which the near-end maneuver stops is indicated as $p_{\mathrm{ne}} \in \mathbb{R}^3 = [15\ 0\ 0]^\top$ (m). Notice that the final target p_{ne} is located 15 m right to the center of the station – whose coordinate in the $\mathcal{F}_{\mathrm{S}}$ system is $[0\ 0\ 0]^\top$ by definition – to comply with the actual position of the docking port.

Because of the above-mentioned evaluation elements, it is deemed it appropriate to perform the subsequent experiments only on the basis of the impulsive-control, variable-speed regulation strategy.

Since in the experiments a disturbance is present even along the y axis, it is interesting to evaluate the effects of such disturbance on the ability of a spacecraft to adhere to the orbital plane. The control strategies do not have as explicit goal to keep the motion of a spacecraft over the vertical $(x - z)$ plane but the final guidance implicitly attains such goal. The Figure 5.21 shows the effects of the disturbances on the y coordinate of the spacecraft in the LVLH reference frame. Worth it to highlight how in the proximity of the first obstacle along the route, corresponds a peak of off-orbit displacement, this result is a consequence of the repulsive force, which is remarkably strong due to the radius of that obstacle, combined with natural y displacement caused by random disturbances.

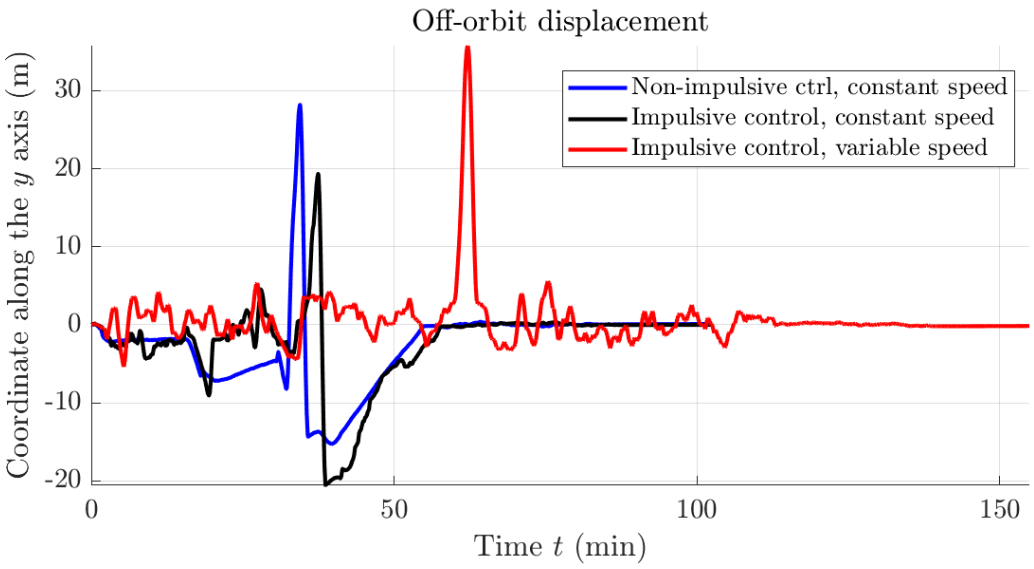

Figure 5.21: Numerical results obtained for the Experiment 1 about cruising phase: Detail of the off-orbit effect caused by random disturbances.

5.2.2 Experiment 2

The aim of the second experiment is to verify the correct behavior of the guidance algorithm of the first experiment in a case of moving obstacles. The same obstacles as *Experiment 1* are now supposed to shift over time in a uniform rectilinear motion by setting an initial speed and a direction angle. Every obstacle is considered moving on the $x-z$ plane in the LVLH coordinate frame. The initial conditions are shown in Table 5.9.

Speed (m/s)	Direction angle (°)
$\nu_1 = 1$ (m/s)	$\theta_1 = 140$ (°)
$\nu_2 = 0.5$ (m/s)	$\theta_2 = -80$ (°)
$\nu_3 = 0$ (m/s)	$\theta_3 = 0$ (°)
$\nu_4 = 0$ (m/s)	$\theta_4 = 0$ (°)

Table 5.9: Speed and direction angles of the obstacles ordered by size. Note that the last two obstacles are not moving.

The Figure 5.22 shows the trajectory of the spacecraft during the cruising phase. As shown in the figure, the algorithm behaves correctly near the obstacles by directing the spacecraft away from the obstacles' motion direction, while it performs as usual for the last two fixed obstacles.

As already described, to ensure the avoidance it is considered a spacecraft endowed with sensors capable to detects debris and other obstacles from enough distance or a spacecraft already provided with the position of each obstacle over time.

No other major differences can be evaluated between this experiment and the previous one because the results about propellant consumption and off-orbit displacement depends majorly on the obstacles' direction and speed.

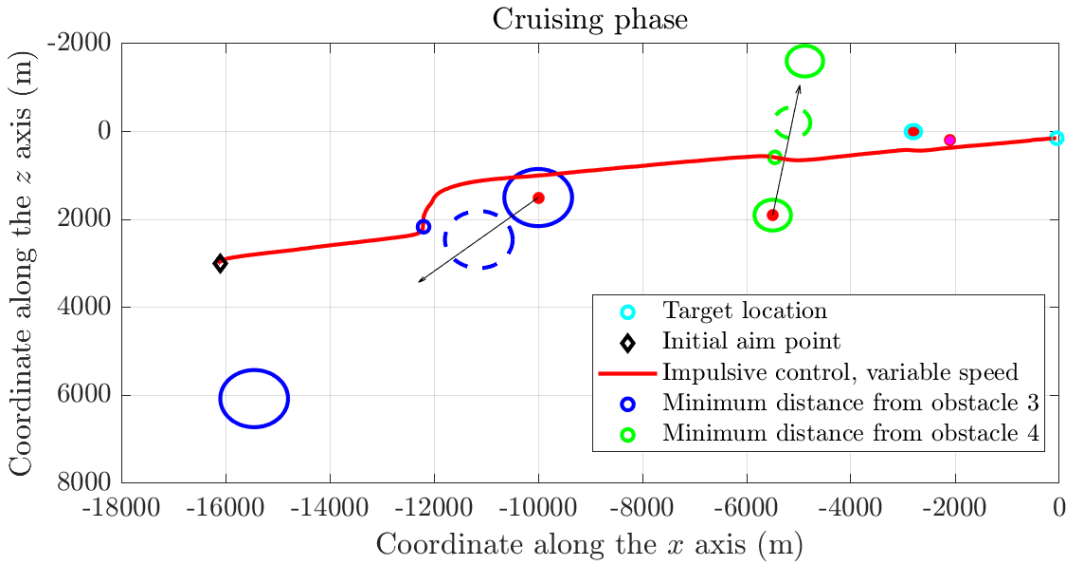

Figure 5.22: Numerical results obtained for the Experiment 2 about cruising phase: Obstacles moving in a uniform rectilinear motion. The blue and green dashed lines represent the position, respectively, of obstacle 3 and obstacle 4, at minimum distance from spacecraft during cruising phase. While the continuous blue and green ovals without a red dot inside are the final positions of moving obstacles.

5.2.3 Experiment 3

The purpose of the third experiment on rendezvous is to evaluate how joint position/orientation regulation affect the performance of spacecraft guidance algorithm.

In the present experiment, random disturbances on the mechanical torque affecting the orientation of the spacecraft are taken into account. In particular, the non-entries of the term T_{rd} are chosen to be zero-mean Gaussian random variables of standard deviation 0.01 N·m.

Four attitude-regulation control torques are tested, corresponding to the cases discussed in Section 4.4. The values of the parameters are chosen to be $K_{\mathrm{S}} = 2.5\, J_{\mathrm{C}}$, $K_{\mathrm{FBP}} = 0.002\, J_{\mathrm{C}}$ and $K_{\mathrm{f}} = 2.5\, J_{\mathrm{C}}$. (As in the previous experiments, the coefficients are parameterized as units or fractions of the inertia coefficients J_{C} for convenience.) The numerical results are illustrated in Figure 5.23, which shows the trajectory of the spacecraft along the $x - z$ plane in the LVLH coordinate frame.

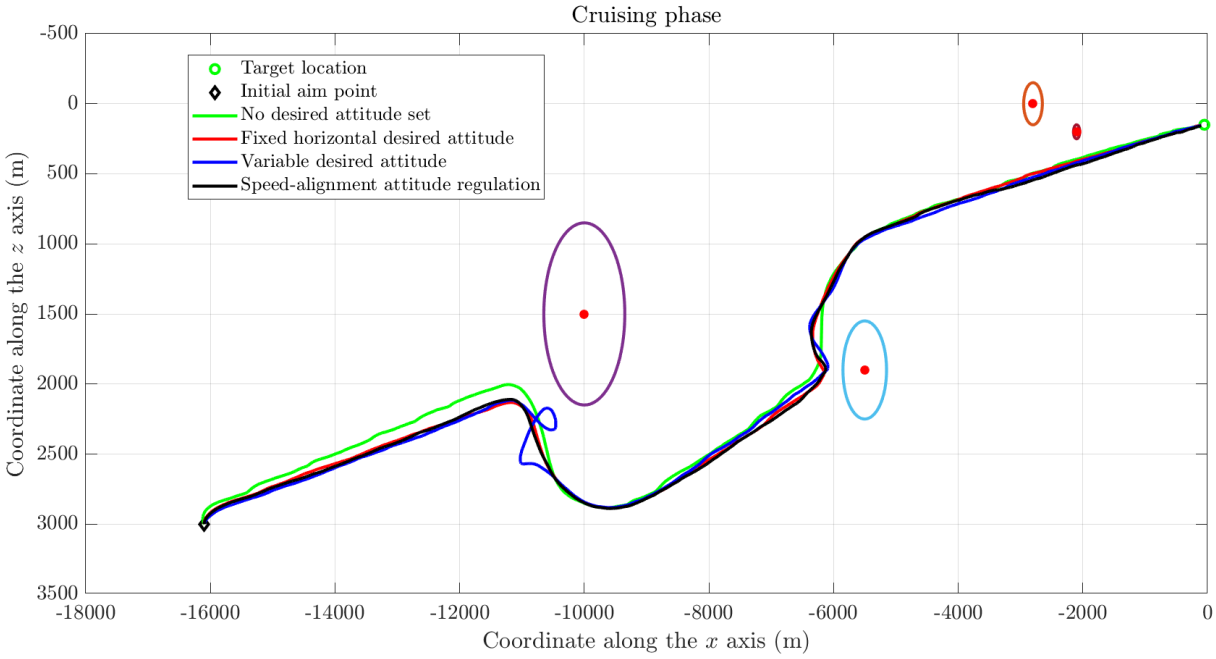

Figure 5.23: Numerical results obtained for the Experiment 3 about cruising phase: Trajectory in the LVLH coordinate frame.

From this figure, it appears clearly that the variable-desired-attitude strategy fails in the proximity of the largest obstacle. On the other hand, the strategy based on not setting a desired attitude, the one based on a fixed (horizontal) attitude and the ones based on velocity alignment perform similarly to one another.

The above results tell that the best performing control strategy corresponds to setting a constant desired attitude (which, in the present endeavor, is chosen to be the docking orientation). It should be, however, recognized that the strategy that entails the least consumption of propellant consists in not operating the reaction wheels at all during the cruising phase, hence leaving the spacecraft at the mercy of inertia and little accidental impacts.

During the docking maneuver, both position and orientation regulation are of prime importance, to guarantee that the spacecraft approaches the docking port of the space station at the right location and with the right orientation.

The Figure 5.24, shows the trajectory of the spacecraft along the $x - z$ plane in the LVLH coordinate frame during a docking phase.

From the figure, it is readily observed that in all cases the trajectory of the spacecraft keeps well behind the safety contour during the far-end-approaching phase, while the near-end-approaching maneuver drives the spacecraft straight behind the docking port.

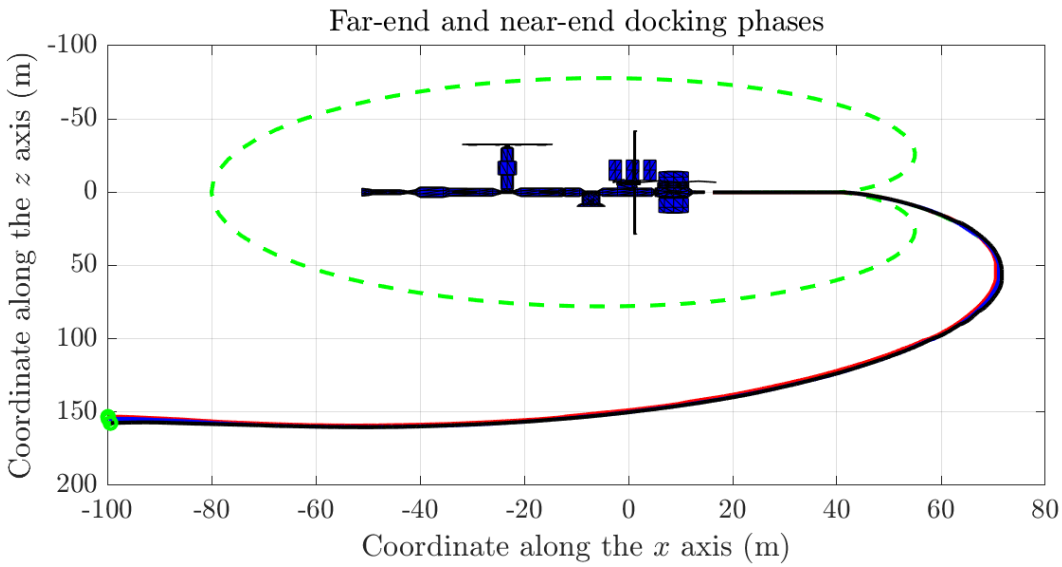

Figure 5.24: Numerical results obtained for the Experiment 3 about docking phase: Trajectory in the LVLH coordinate frame. (Since the Z axis actually points toward the Earth, the picture looks upside down.) The dashed green line represent the safety cardioid-shaped contour that the spacecraft should keep out of.

As a further element of evaluation, the Figure 5.25, shows the velocity of the spacecraft along the x axis and along the z axis in the LVLH coordinate frame during the whole rendezvous maneuver.

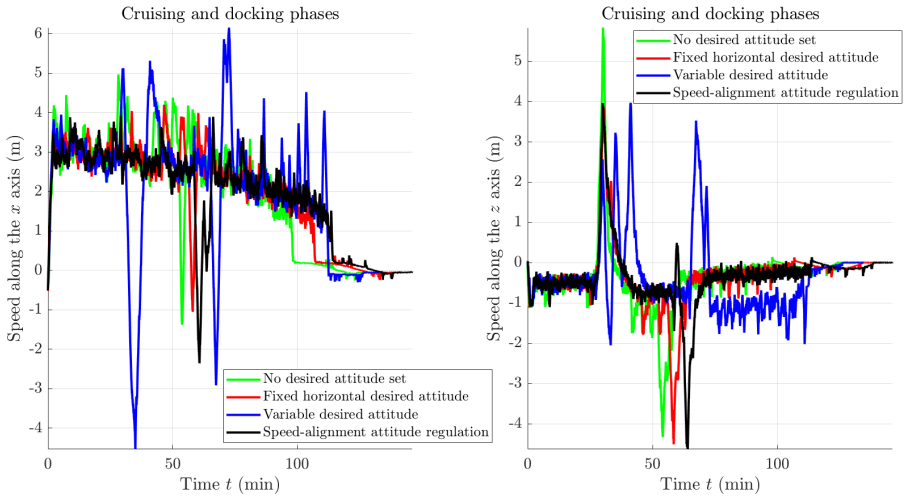

Figure 5.25: Numerical results obtained for the Experiment 3 about rendezvous: Velocity of the spacecraft in the LVLH coordinate frame.

The velocity curves corresponding to a variable-speed, impulsive control strategy in connection with the four discussed orientation regulation methods show that the no-desired-attitude

and the variable-desired-attitude methods stand out negatively. Such methods, as a matter of fact, cause a sudden rise of velocity in the proximity of large obstacles.

The Figure 5.26, shows the consumption of propellant during the whole rendezvous maneuver. Vertical lines within the figure stand as delimiters of the three different phases of rendezvous (cruising, far-end approach and near-end approach).

From the mass-decay curves emerges that most propellant is consumed during the cruising phase. Also, the curves show that the fixed-horizontal-attitude strategy causes the most limited consumption of propellant during the entire rendezvous maneuver.

In addition to the above elements to evaluate the behavior of the control strategies under examination, the Figure 5.27 shows the orientation of the spacecraft along the entire rendezvous maneuver in terms of Euler angles computed on the basis of the instantaneous attitude matrix-indicator R.

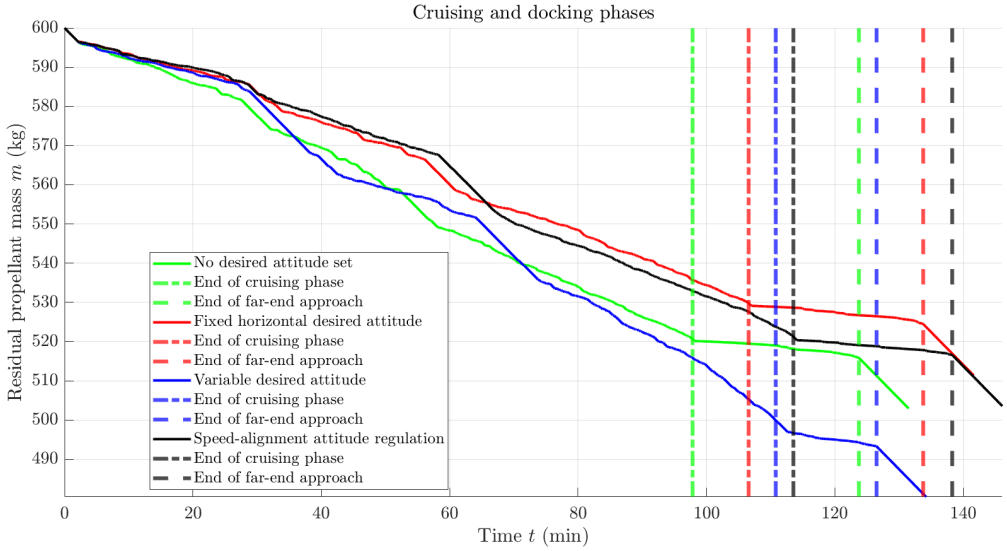

Figure 5.26: Numerical results obtained for the Experiment 3 about rendezvous: Propellant consumption.

It is immediate to notice that the speed-alignment-based attitude control strategy does not stand as particularly appealing as it leads to a very low convergence rate and, if sped up, entails an excessive disturbance to the navigation algorithm.

It is important to remark that the choice of a constant desired attitude is possible only if the spacecraft is provided with a sufficient number of on-board proximity sensor positioned all over the spacecraft, if that is not possible due to different reasons, the best choice would be to let the chaser pointing always toward the space station, but this strategy has not been elaborated in the present thesis.

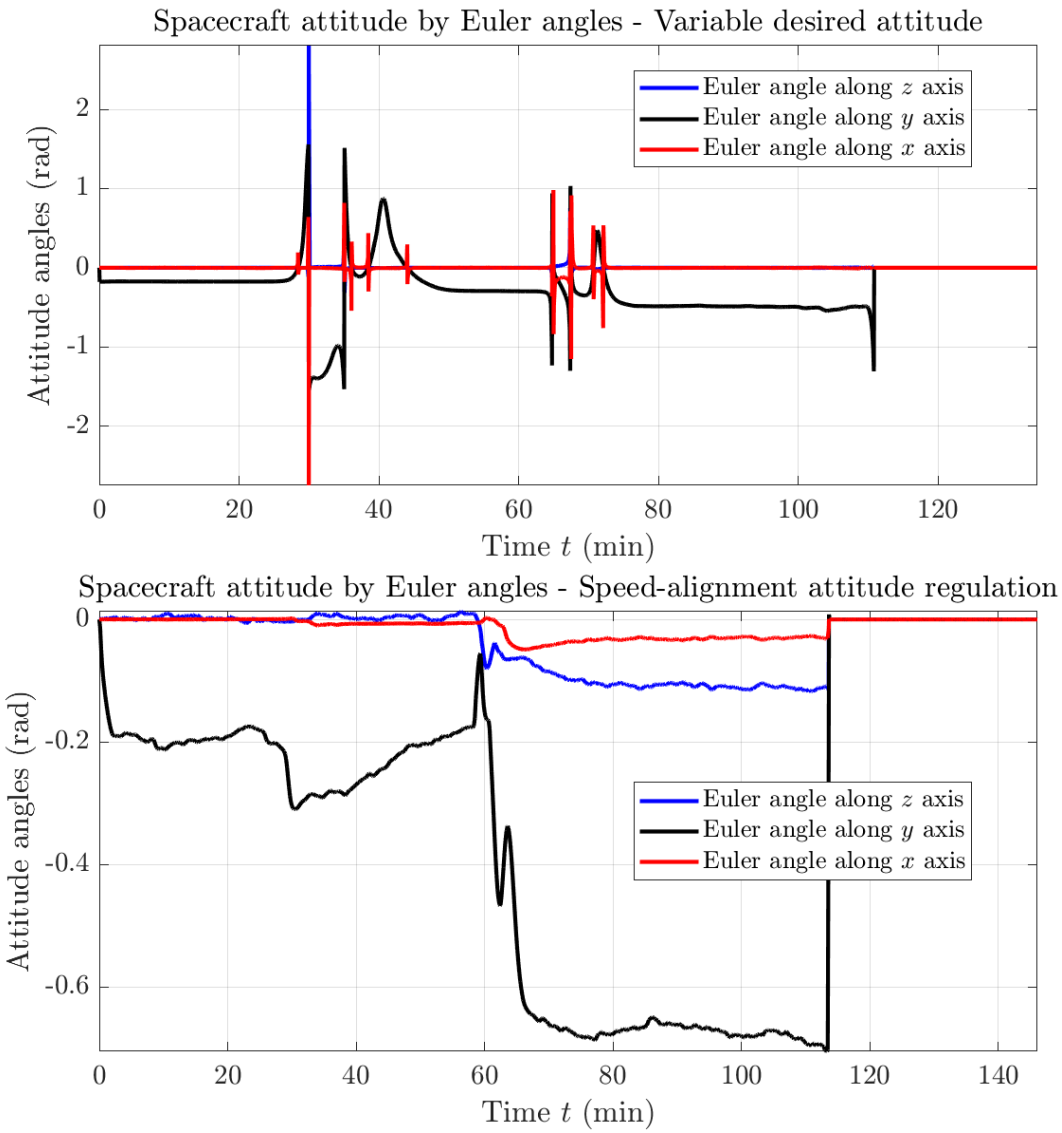

Figure 5.27: Numerical results obtained for the Experiment 3 about rendezvous: Euler angles computed on the basis of the instantaneous attitude matrix-indicator R.

5.3 Illustration of a complete rendezvous maneuver

From the previous evaluated experiments, a complete maneuver is performed from initial aim point to a docking port through cruising, far-end approaching and near-end approaching.

Figure 5.28 illustrates the cruising and docking phases. Shown result is performed using the variable-speed impulsive control algorithm explained in Section 4.3 and, for attitude control, fixed horizontal desired attitude strategy described in Section 4.4, these already mentioned strategies are the most suitable for cruising phase among the ones studied in this thesis (weaknesses and strengths are evaluated in *Experiment 1* and *Experiment 3*). The far-end and near-end phases

are performed as described in Sections 4.5 and 4.6. All constants used come from *Experiment 3*.

From the figure below is clear that a smooth trajectory is performed across the obstacles and around the space station, while the spacecraft keeps enough far from the radii of the obstacles and from the cardioid region. A fixed attitude control strategy is able to point the spacecraft toward the docking axis and, as seen in *Experiment 3*, to reduce the propellant consumption. Hence, the solution obtained ensures a steady rendezvous and a stable trajectory during all three phases.

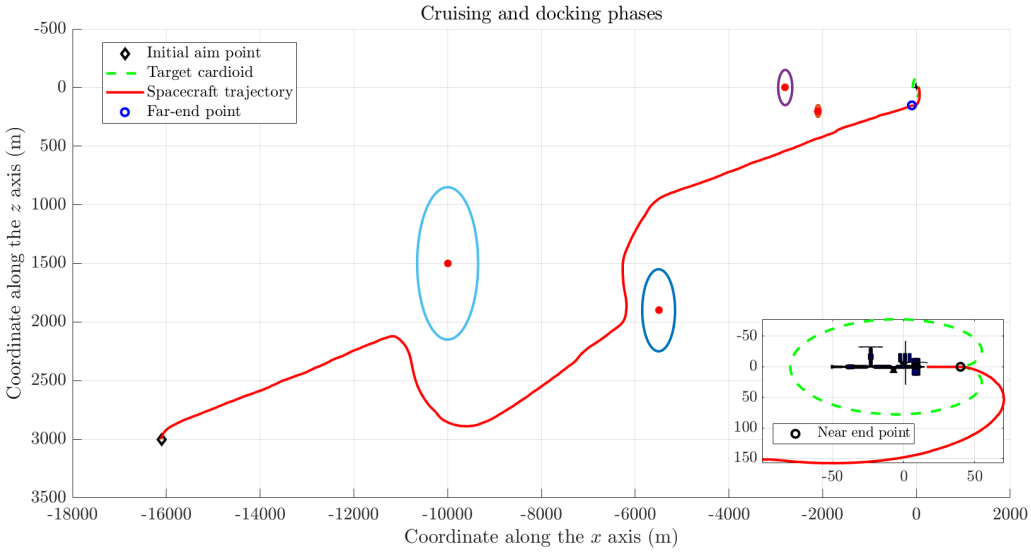

Figure 5.28: Complete rendezvous from initial point to docking port: Trajectory in the LVLH coordinate frame. The main plot shows the complete trajectory from the initial aim point to the arrival docking port, while the box is a zoom in of far-end and near-end approaching.

Chapter 6

Conclusion

The aim of the present thesis was to propose a framework to model, simulate and control a small unmanned spacecraft, orbiting in close proximity of a space station, through manifold calculus. Two maneuvers were modeled and simulated, that is, reorientation under directional constraints and rendezvous in the presence of fixed as well as moving obstacles.

Obstacle avoidance was traditionally considered a high-level planning problem, while in recent research endeavors part of such task has been shown to be manageable by real-time low-level control algorithms [31]. The present thesis follows such modern line of research and is based on multi-objective optimization.

The main theoretical instrument utilized in the present thesis is that of virtual attractive-repulsive potential. In fact, a physical object moves in a force field derived as anti-gradient of a potential function which embodies localized information about the spacecraft to be guided and the surrounding environment. It was believed that the complexity of tasks that can be tackled by means of this approach is limited, because of local minima in the potential function [31] which may lead a controlled object to a stable configuration different from the intended goal. However, it has been shown even by the present contribution that virtual-potential-based guidance, if properly designed and tuned, shows the ability to lead to acceptable results under reasonable tolerance levels.

A distinguishing feature of the present thesis is that, unlikely most research papers in the area that invoke the use of coordinates or quaternions, the mathematical model of the roto-translational motion of a spacecraft as well as the design of control fields were written in a coordinate-free Lie-group-type notation.

A number of numerical experiments, aimed at complementing the theoretical developments, were discussed to illustrate the achieved progress and to guide the reader though a series of evaluations. Such evaluation stages were aimed at establishing which control strategy, among various possible combinations, appears to be the most convenient one.

During the development of the present thesis, a number of minor issues emerged which would need a closer examination.

An aspect to pay attention to is the effect of repulsive fields far away from the obstacles, both physical and directional, which may drive a spacecraft slightly off-track with respect to the intended target. Such problem has been dealt with by tuning the constant parameters in the guidance algorithm, although a hard-limiting strategy would perhaps prove more effective as it would cut off completely the repulsive fields whenever sufficiently far from their source.

A further aspect to pay attention to concerns alignment of a spacecraft attitude to a docking axis during final guidance in a robust way. Currently, final guidance is performed by setting up a torque term that tends to keep the reference frame $\mathcal{F}_{\mathrm{C}}$ aligned to the frame $\mathcal{F}_{\mathrm{S}}$ irrespective of possible orientation constraints or disturbances. Attitude control during such phase may be made more robust by introducing mandatory as well as forbidden directions and by enriching the torque control field by components related to such directional constraints.

Chapter 7

Appendix

In a computer code, a unit quaternion denotes a point on a 4D hypersphere S^3 and a 3D rotation matrix denotes an element on the special orthogonal group $\mathrm{SO}(3)$ up to machine precision. While a rotation matrix is seldom expressed directly through its numerical entries, a quaternion often is. When the entries of a quaternion are described by a small number of digits, e.g., by four decimal digits, its conversion to a rotation matrix does not result in a true rotation. The conversion of a quaternion $[q_i \; q_j \; q_k \; q_0]^\top$ written in JPL notation to a rotation matrix R may be expressed as

$$\tilde{R} = \begin{bmatrix} 1 - 2(q_j^2 + q_k^2) & 2(q_i q_j - q_k q_0) & 2(q_i q_k + q_j q_0) \\ 2(q_i q_j + q_k q_0) & 1 - 2(q_i^2 + q_k^2) & 2(q_j q_k - q_i q_0) \\ 2(q_i q_k - q_j q_0) & 2(q_j q_k + q_i q_0) & 1 - 2(q_i^2 + q_j^2) \end{bmatrix},$$

where q_0 denotes the real part of the quaternion. To fix non-unitarity, it is added a projection to the $\mathrm{SO}(3)$ group based on singular value decomposition (SVD), namely

$$UDV^\top = \tilde{R}, \; R := UV^\top,$$

where U, V denote the orthogonal factors of the SVD.

Bibliography

[1] I. Lopez and C. R. McInnes. "Autonomous rendezvous using artificial potential function guidance". In: *Journal of Guidance, Control, and Dynamics* 18.2 (1995), pp. 237–241. DOI: 10.2514/3.21375.

[2] N. Bloise et al. "Obstacle avoidance with potential field applied to a rendezvous maneuver". In: *Applied Sciences* 7.10 (2017). ISSN: 2076-3417. DOI: 10.3390/app7101042.

[3] A. Bongers and J. Torres. "Orbital debris and the market for satellites". In: *Ecological Economics* 209 (2023). ISSN: 0921-8009. DOI: https://doi.org/10.1016/j.ecolecon.2023.107831.

[4] C. R. Mclnnes. "Large angle slew maneuvers with autonomous sun vector avoidance". In: *Journal of Guidance, Control, and Dynamics* 17.4 (1994), pp. 875–877. DOI: 10.2514/3.21283.

[5] Q. Hu, B. Chi, and M. R. Akella. "Anti-unwinding attitude control of spacecraft with forbidden pointing constraints". In: *Journal of Guidance, Control, and Dynamics* 42.4 (2019), pp. 822–835. DOI: 10.2514/1.G003606.

[6] H. B. Hablani. "Attitude commands avoiding bright objects and maintaining communication with ground station". In: *Journal of Guidance, Control, and Dynamics* 22.6 (1999), pp. 759–767. DOI: 10.2514/2.4469.

[7] U. Lee and M. Mesbahi. "Feedback control for spacecraft reorientation under attitude constraints via convex potentials". In: *IEEE Transactions on Aerospace and Electronic Systems* 50.4 (2014), pp. 2578–2592. DOI: 10.1109/TAES.2014.120240.

[8] R. E. Roberson and R. Schwertassek. *Dynamics of multibody systems*. Springer-Verlag Berlin Heidelberg, 1988.

[9] H. Cheng and K. C. Gupta. "An historical note on finite rotations". In: *Journal of Applied Mechanics* 56.1 (1989), pp. 139–145. ISSN: 0021-8936. DOI: 10.1115/1.3176034.

[10] S. Fiori. "Model formulation over Lie groups and numerical methods to simulate the motion of gyrostats and quadrotors". In: *Mathematics* 7.10 (2019). ISSN: 2227–7390. DOI: 10.3390/math7100935. URL: https://www.mdpi.com/2227-7390/7/10/935.

[11] S. Fiori et al. “Extension of a PID control theory to Lie groups applied to synchronising satellites and drones”. In: *IET Control Theory & Applications* 14 (17 2020), pp. 2628–2642. ISSN: 1751-8644.

[12] S. Fiori and L. Del Rossi. “Minimal control effort and time Lie-group synchronisation design based on proportional-derivative control”. In: *International Journal of Control* 1 (2022), pp. 138–150. DOI: 10.1080/00207179.2020.1780474. URL: https://doi.org/10.1080/00207179.2020.1780474.

[13] J. L. Baxter et al. “Multi-robot search and rescue: A potential field based approach”. In: *Autonomous Robots and Agents*. Ed. by S. C. Mukhopadhyay and G. S. Gupta. Berlin, Heidelberg: Springer Berlin Heidelberg, 2007, pp. 9–16. ISBN: 978-3-540-73424-6. DOI: 10.1007/978-3-540-73424-6_2. URL: https://doi.org/10.1007/978-3-540-73424-6_2.

[14] E. Rimon and D. Koditschek. “Exact robot navigation using artificial potential functions”. In: *IEEE Transactions on Robotics and Automation* 8.5 (1992), pp. 501–518.

[15] S. Shimoda, Y. Kuroda, and K. Iagnemma. “Potential field navigation of high speed unmanned ground vehicles on uneven terrain”. In: *Proceedings of the 2005 IEEE International Conference on Robotics and Automation*. 2005, pp. 2828–2833. DOI: 10.1109/ROBOT.2005.1570542.

[16] L. Huang. “Velocity planning for a mobile robot to track a moving target – A potential field approach”. In: *Robotics and Autonomous Systems* 57.1 (2009), pp. 55–63. ISSN: 0921-8890. DOI: https://doi.org/10.1016/j.robot.2008.02.005.

[17] I. Kamon, E. Rimon, and E. Rivlin. “TangentBug: A range-sensor-based navigation algorithm”. In: *The International Journal of Robotics Research* 17.9 (1998), pp. 934–953. DOI: 10.1177/027836499801700903.

[18] I. Kamon and E. Rivlin. “Sensory-based motion planning with global proofs”. In: *IEEE Transactions on Robotics and Automation* 13 (1997), pp. 814–822.

[19] D. Koditschek and E. Rimon. “Robot navigation functions on manifolds with boundary”. In: *Advances in Applied Mathematics* 11.4 (1990), pp. 412–442.

[20] M. C. Lee and M. G. Park. “Artificial potential field based path planning for mobile robots using a virtual obstacle concept”. In: *Proceedings of the 2003 IEEE/ASME International Conference on Advanced Intelligent Mechatronics (AIM 2003)*. Vol. 2. 2003, pp. 735–740. DOI: 10.1109/AIM.2003.1225434.

[21] E. Leonard and E. Fiorelli. “Virtual leaders, artificial potentials and coordinated control of groups”. In: *Proceedings of the 40th IEEE Conference on Decision and Control* (2001), pp. 2968–2973.

[22] H. Levine, W.-J. Rappel, and I. Cohen. “Self-organization in systems of self-propelled particles”. In: *Physical Review E* 63 (2000).

[23] Y. Rasekhipour et al. “A potential field-based model predictive path-planning controller for autonomous road vehicles”. In: *IEEE Transactions on Intelligent Transportation Systems* 18.5 (2017), pp. 1255–1267. DOI: 10.1109/TITS.2016.2604240.

[24] B. Nguyen et al. “Virtual attractive-repulsive potentials for cooperative control of second order dynamic vehicles on the Caltech MVWT”. In: *Proceedings of the 2005 American Control Conference*. (Portland, OR, USA), June 2005, pp. 1084–1089.

[25] S. Fiori, L. Bigelli, and F. Polenta. “Lie-group type quadcopter control design by dynamics replacement and the virtual attractive-repulsive potentials theory”. In: *Mathematics* 10.7 (Mar. 2022), p. 1104. ISSN: 2227-7390. DOI: 10.3390/math10071104. URL: http://dx.doi.org/10.3390/math10071104.

[26] A. Bloch et al. “Stabilization of rigid body dynamics by internal and external torques”. In: *Automatica* 28.4 (1992), pp. 745–756. ISSN: 0005-1098. DOI: https://doi.org/10.1016/0005-1098(92)90034-D.

[27] W. Clohessy and R. Wiltshire. “Terminal guidance system for satellite rendezvous”. In: *Journal of the Aerospace Sciences* 27.9 (1960), pp. 653–658. DOI: 10.2514/8.8704.

[28] J. Ries et al. “Progress in the determination of the gravitational coefficient of the Earth”. In: *Geophysical Research Letters* 19.6 (1992), pp. 529–531.

[29] D. Schneider. “Non-holonomic Euler-Poincaré equations and stability in Chaplygin’s sphere”. In: *Dynamical Systems* 17.2 (2002), pp. 87–130. DOI: 10.1080/02681110110112852.

[30] G. Sutton and O. Biblarz. *Rocket Propulsion Elements – An introduction to the engineering of rockets*. 7th ed. Wiley-Interscience, 2000.

[31] O. Khatib. “Real-time obstacle avoidance for manipulators and mobile robots”. In: *The International Journal of Robotics Research* 5.1 (1986), pp. 90–98. DOI: 10.1177/027836498600500106.

[32] S. Fiori. “Manifold calculus in system theory and control – Fundamentals and first-order systems”. In: *Symmetry* 13.11 (Nov. 2021), p. 2092. ISSN: 2073-8994. DOI: 10.3390/sym13112092. URL: http://dx.doi.org/10.3390/sym13112092.

[33] S. Fiori. “Manifold calculus in system theory and control – Second order structures and systems”. In: *Symmetry* 14.6 (June 2022), p. 1144. ISSN: 2073-8994. DOI: 10.3390/sym14061144. URL: http://dx.doi.org/10.3390/sym14061144.

[34] R. S. Chandrasekaran et al. “Variational collision and obstacle avoidance of multi-agent systems on Riemannian manifolds”. In: *2020 European Control Conference (ECC)*. 2020, pp. 1689–1694. DOI: 10.23919/ECC51009.2020.9143986.

[35] G. Wang et al. “Docking strategy for a space station container docking device based on adaptive sensing”. In: *IEEE Access* 7 (2019), pp. 100867–100880. DOI: 10.1109/ACCESS.2019.2930558.

[36] H. Gong et al. “Analysis of docking tolerance capability of underwater tool-switching device”. In: *Journal of Physics: Conference Series* 1748.6 (2021), p. 062045. DOI: 10.1088/1742-6596/1748/6/062045.

[37] S. Paternain, D. E. Koditschek, and A. Ribeiro. “Navigation functions for convex potentials in a space with convex obstacles”. In: *IEEE Transactions on Automatic Control* 63.9 (2018), pp. 2944–2959. DOI: 10.1109/TAC.2017.2775046.

[38] A. Bartoszewicz and J. Żuk. “Sliding mode control — Basic concepts and current trends”. In: *2010 IEEE International Symposium on Industrial Electronics*. 2010, pp. 3772–3777. DOI: 10.1109/ISIE.2010.5637990.

[39] S. Spurgeon. “Sliding mode control: a tutorial”. In: *2014 European Control Conference (ECC)*. 2014, pp. 2272–2277. DOI: 10.1109/ECC.2014.6862622.

[40] V. Utkin. “Sliding mode control design principles and applications to electric drives”. In: *IEEE Transactions on Industrial Electronics* 40.1 (1993), pp. 23–36. DOI: 10.1109/41.184818.

Acknowledgements

I would like to express my gratitude to my supervisor, Prof. Fiori Simone, who assisted and guided me throughout this project and whom without this would have not been possible. I would also thank him for the abroad traineeship experience he made possible.

I would like to gratefully thank Prof. Toshihisa Tanaka (Tokyo University of Agriculture and Technology – TUAT, Japan) for hosting me at the Department of Electrical and Electronic Engineering of the TUAT (Koganei campus) during March – May, 2023.

I would like to thank Sabatini Luca and Rachiglia Francesco with whom I spent my best days abroad.

Lastly, I would like to thank my family, whom without this would have not been possible.